

Article

Interactions between Clays and Carbonates in the Aptian Pre-Salt Reservoirs of Santos Basin, Eastern Brazilian Margin

Argos Belmonte Silveira Schrank ^{1,2,*}, Thisiane Dos Santos ², Sabrina Danni Altenhofen ², William Freitas ², Elias Cembrani ¹, Thiago Haubert ², Felipe Dalla Vecchia ², Rosalia Barili ², Amanda Goulart Rodrigues ¹, Anderson Maraschin ² and Luiz Fernando De Ros ¹

¹ Instituto de Geociências, Campus do Vale. Federal University of Rio Grande do Sul (UFRGS), Av. Bento Gonçalves, 9500 Agronomia, Porto Alegre 90650-001, Brazil;

elias.cembrani@petrobras.com.br (E.C.); goulart.rodrigues@ufrgs.br (A.G.R.); lfderos@inf.ufrgs.br (L.F.D.R.)

² Institute of Petroleum and Natural Resources (IPR), Building 96J, Pontifical Catholic University of Rio Grande do Sul (PUCRS), Av. Ipiranga, 6681-Partenon, Porto Alegre 90619-900, Brazil; thisiane.santos@pucrs.br (T.D.S.); sabrina.altenhofen@pucrs.br (S.D.A.); william.freitas@pucrs.br (W.F.); thiago.haubert@pucrs.br (T.H.); felipe.vecchia@pucrs.br (F.D.V.); rosalia.cunha@pucrs.br (R.B.); anderson.maraschin@pucrs.br (A.M.)

* Correspondence: argosssb@hotmail.com

Abstract: The giant Pre-salt reservoirs represent most of the oil production in Brazil. The main Aptian sag reservoirs were deposited in a unique and highly complex hyper-alkaline lacustrine setting. These deposits are essentially constituted by fascicular and spherulitic calcite precipitated in a magnesian clay matrix (stevensite, kerolite, and saponite/hectorite). Although vital for understanding the origin and main reservoir quality control, the genesis and interactions of clays and carbonates are still poorly constrained. The detailed petrographic description was focused on 812 thin sections from five wells drilled in the Santos Basin Aptian Barra Velha Formation, combined with cathodoluminescence, UV epifluorescence, and X-ray diffraction analyses. The main syngenetic processes were the deposition of finely laminated peloidal and ooidal Mg-clays, the formation of fascicular calcite crusts on the sediment–water interface, and the redeposition of these materials as intraclasts. Abundant clay peloids engulfed in syngenetic shrubs indicate that calcite and clay precipitation was concomitant, though with highly variable rates. Eodiagenetic phases include matrix-replacive and -displacive spherulites and fascicular shrubs; matrix-replacive blocky calcite and dolomite; lamellar carbonates filling matrix shrinkage pores; and microcrystalline calcite, dolomite, and silica replacing the Mg-clay matrix. The preferential dolomitization and calcitization of peloidal layers were most likely due to their higher permeability and larger specific surface. Matrix-replacive saddle dolomite, macrocrystalline calcite, and dawsonite are interpreted as mesodiagenetic or hydrothermal phases after significant matrix dissolution. Unraveling the processes of the formation and alteration of the carbonates and clays and their interactions in the Pre-salt deposits is essential for constraining the depositional and diagenetic conditions in their unique environments and their diagenetic overprinting and for decreasing the exploration risks and increasing the production of those extraordinary reservoirs.

Keywords: Pre-salt; Aptian; carbonate–clay interactions; Barra Velha Formation; Santos Basin; diagenesis



Citation: Schrank, A.B.S.; Dos Santos, T.; Altenhofen, S.D.; Freitas, W.; Cembrani, E.; Haubert, T.; Dalla Vecchia, F.; Barili, R.; Rodrigues, A.G.; Maraschin, A.; et al. Interactions between Clays and Carbonates in the Aptian Pre-Salt Reservoirs of Santos Basin, Eastern Brazilian Margin. *Minerals* **2024**, *14*, 191. <https://doi.org/10.3390/min14020191>

Academic Editor: János Haas

Received: 20 December 2023

Revised: 7 January 2024

Accepted: 16 January 2024

Published: 11 February 2024



Copyright: © 2024 by the authors. Licensee MDPI, Basel, Switzerland. This article is an open access article distributed under the terms and conditions of the Creative Commons Attribution (CC BY) license (<https://creativecommons.org/licenses/by/4.0/>).

1. Introduction

The giant oil and gas accumulations in Aptian lacustrine reservoirs in eastern Brazilian basins and their western African counterparts along the South Atlantic conjugate margins, known as the Pre-salt deposits [1–6], represent some of the most important discoveries of this century. These rocks represent a unique combination of calcite aggregates, magnesian phyllosilicates, dolomite, and silica. Their origin and evolution are matters of ongoing discussion in the scientific community on topics such as the mechanisms of carbonate formation, the degree and importance of microbial or biotic processes in their precipitation,

the controls on facies deposition and distribution, the nature of the alkaline lacustrine fluids, and the timing and controls in diagenetic alterations (e.g., [5,7–25]). There is, unfortunately, no ancient or modern analog that encompasses the environment, size, and composition of the South Atlantic Pre-salt deposits. This makes it difficult to interpret the processes of the formation and distribution of Pre-salt deposits.

The substrate of the Pre-salt rocks that formed in situ was essentially composed originally of magnesian clays, with spherulitic and fascicular calcite aggregates forming shortly after deposition in varying sizes, distributions, and proportions (e.g., [8,10,16,23–25]). Carbonates represent the main Pre-salt diagenetic phases formed in a Mg-clay matrix background [16,23,25]. Many in situ Pre-salt rocks show high porosity and permeability as a result of extensive Mg-clay dissolution, identified as their main porosity-generating process [21,24,26]. Understanding the relationships between carbonates and Mg-clays is of the utmost importance for defining the genesis and evolution of the unique Pre-salt rocks, as well as the main controls on the generation and distribution of porosity in the reservoirs.

Despite the great importance of carbonates and clay minerals in controlling reservoir quality, the geochemical and environmental conditions responsible for their formation are still poorly understood. Few studies examined the fundamental relationships between carbonates and Mg-clays in the Pre-salt deposits. Besides controlling reservoir quality, carbonate–clay interactions reveal important information on the depositional processes and diagenetic evolution of these important reservoirs.

In the current study, we aim to explore the complex and diverse interactions between carbonate and Mg-clay phases in order to better understand their distribution and potential formation mechanisms. The acquired results allowed us to unravel the mechanisms involved in the formation and evolution of the complex Pre-salt sag deposits.

2. Geologic Context

The Santos Basin (Figure 1) is one of the largest Brazilian marginal basins, with around 350,000 km², extending eastward to more than 3000 m water depth [27]. The basin is limited to the north by the Cabo Frio High, with the Campos Basin, and to the south by the Florianópolis High, with the Pelotas Basin [27,28]. Its stratigraphy is divided into three stages or super sequences [27], i.e., rift, post-rift, and drift.

The rift super sequence corresponds to the basaltic volcanic rocks of the Early Cretaceous Camboriú Formation that overly a granitic–gneissic Precambrian basement, to the Barremian siliciclastic alluvial conglomerates and lacustrine talc-stevensitic sandstones and mudstones of the Piçarras Formation and to the late Barremian to early Aptian bioclastic calcirudites and calcarenites and organic shales of the Itapema Formation. The top of this super sequence is defined by a widespread erosive surface called the Pre-Alagoas unconformity [27] (Figure 2).

The post-rift stage is related to a phase when thermal subsidence was the predominant mechanism, creating a large, relatively flat, and shallow, sag-type basin [29,30]. The post-rift super sequence, the focus of this study, is constituted by the early Aptian Barra Velha Formation (BVF), consisting of carbonate-Mg-clay rocks, and by the late Aptian Ariri Formation evaporites (Figure 2). The deposition of the BVF was originally interpreted as microbial by Terra et al. [7] and Dias [31] and later reinterpreted as a result of abiotic precipitation in evaporative lacustrine conditions by Wright and Barnett [8]. The main BVF deposits are composed of a combination of in situ fascicular and spherulitic calcites and Mg-clay matrices and of rocks composed of the reworked fragments of carbonate aggregates. The topmost section of the Aptian interval is represented by the Ariri Formation, which represents an extensive layered sequence of anhydrite, halite, and other chlorides, locally larger than 2 km thick [27]. These evaporites mark the large-scale entrance of seawater into the sag lake system, representing a massive marine transgression [27,32].

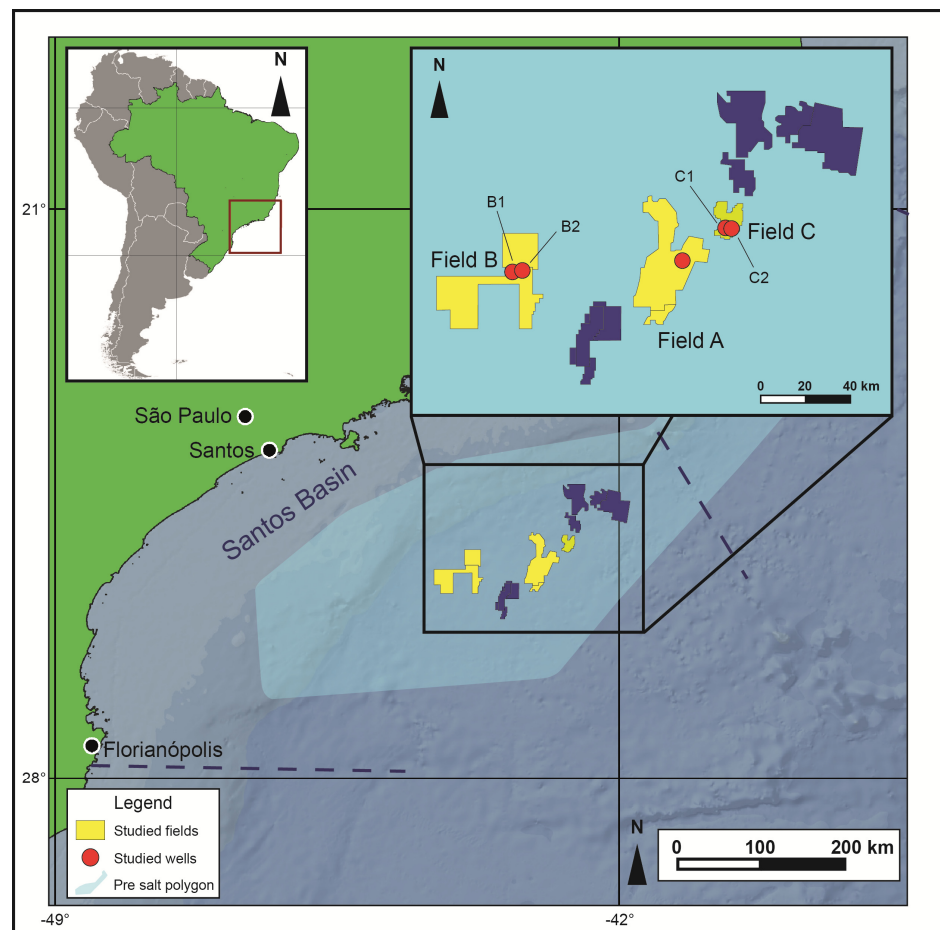


Figure 1. Location map showing the studied wells in red.

Chronostratigraphy			Stage	Lithostratigraphy	Unconformities	
Lower Cretaceous	Aptian	(Ma)	Alagoas	Guaratiba Group	Ariari	Salt base
		115				
	Barremian	125	Jiquiá		Itapema	Pre-Alagoas
			Buracica		Piçarras	Top Lower Rift
		129.4	Aratu		Camboriú	Basalt Top
	Hauterivian					

Figure 2. Lower Cretaceous stratigraphic chart for the Santos Basin (modified from Wright and Barnett [21] and Moreira et al. [27]).

The drift stage is characterized by the generation of oceanic crust [32] and the individualization of the South American and African plates [33]. Faulting and deformation related to halokinesis are also important during this stage [32], characterized by shallow and deep marine deposition.

3. Materials and Methods

The faciological description of 141.5 m of cores from five wells from three fields in the Santos Basin (Figure 1) was conducted with support of the petrographic characterization of thin sections. Core and petrographic descriptions served as the basis for new sampling for thin section preparation. The exact location and identification of the studied wells and fields are proprietary information and, therefore, cannot be revealed. The wells are identified as well A from field A, wells B1 and B2 from field B, and wells C1 and C2 from field C. Cores and thin sections from wells A, B1, and C1 were described, while B2 and C2 only had thin sections available. Facies were classified according to De Ros and Oliveira [34].

Petrographic analysis of 812 thin sections was performed by counting 300 points along transects perpendicular to the depositional structure and through visual estimation [35,36], both using the Petroledge[®] Workstation software version 3.11.8.1111 [37]. Samples were stained with an alizarine red S and potassium ferricyanide solution [38] in order to differentiate carbonate minerals. Petrographic analysis was conducted with Zeiss Axio ImagerA1 (Zeiss, Gottingen, Germany) and Leica DM750P (Leica, Heerbrugg, Switzerland) polarized transmitted light microscopes. The in situ and reworked samples were classified according to De Ros and Oliveira [34] for the Aptian pre-salt deposits. Fifteen samples were selected for cathodoluminescence (CL) and epifluorescence (EPI) analysis in order to further characterize clay minerals and carbonates. CL analysis was conducted with a Cambridge Image Technology Ltd. (CITL, Hatfield, UK) CL8200 Mk5-2 optical cathodoluminescence cold cathode system mounted on a Zeiss Axioscope 5 (Zeiss, Suzhou, China), with a CITL 2 stage vacuum pump (CITL, Hatfield, UK). EPI analysis used a ZEISS HXP 120 V metal halide fluorescence light source (Zeiss, Jena, Germany) connected to an Axio Imager A2 microscope (Zeiss, Jena, Germany), using a Zeiss ultraviolet set 02 (excitation G 365 nm, beamsplitter FT 395 nm, emission LP 420 nm) and blue-cyan Lumar 09 (excitation BP 450–490 nm, emission LP 515 nm) filters.

Bulk rock and clay fractions were analyzed with a Bruker D8 Advance X-ray Diffractometer (XRD) (Bruker, Karlsruhe, Germany) with Cu α tube (40 kV and 30 mA). The samples were crushed with an agate mortar and pestle and sifted through a 270-mesh sieve. For clay fraction analysis, twenty-nine samples were selected and first suspended in deionized water using a magnetic stirrer with an added deflocculant and later centrifuged at 750 rpm for 7 min; afterward, the supernatant was then further centrifuged for an additional 30 min at 3000 rpm and left to settle. The settled material was then smeared on a glass slide and analyzed with three different treatments: air-dried, saturated with ethylene glycol for 15 h, and heated to 550 °C for 5 h in an oven. Heated samples were further solvated with glycerol and re-heated (cf. Christidis and Koutsopoulou [39]) in order to identify stevensite and saponite–hectorite. Total powder fraction and air-dried slides analysis encompassed 3–90°2 θ with a 0.015°2 θ step size and 0.2 s/step count time. Heated, glycolated, and re-heated slide analysis ranged from 3 to 35°2 θ . Diffractograms were interpreted utilizing Bruker's DIFFRAC.EVA software version 5.2.0.5 with the ICDD Powder Diffraction File[™] 4+ database.

4. Core Descriptions

The main identified facies of the described well cores are summarized in Figures 3 and 4. The facies description and distribution of the A, B1, and C1 cores are summarized in Table 1 and Figure 5.

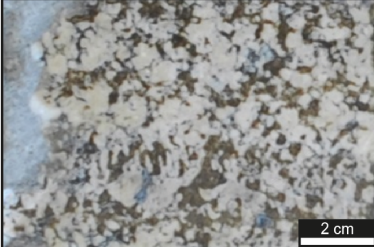
<i>in situ</i>		SHR Shrubstone	Milimetric to centimetric coalesced shrubs with irregular stratification, locally forming crusts within other lithofacies. Inter-aggregate and vugular pores are common.
		MSH Muddy Shrubstone	Shrubs and mud presenting massive texture or rare and incipient irregular lamination. Shrubs are non-coalescent to partially coalescent. Inter-aggregate pores are common while intra-aggregate pores are rare.
		SPH Spherulstone	Coalescent to partially coalescent millimetric spherulites often silicified and dolomitized. Inter-aggregate and vugular pores are common to less common and intra-aggregate pores locally occur.
		MSP Muddy Spherulstone	Non-coalescent to partially coalescent spherulites, with significant amounts of mud, generally displaying incipient irregular or plane-parallel laminations. Trace inter-aggregate pores.
		SSP Shrub- spherulstone	Shrubs and spherulites dispersed in mud matrix or with high frequency intercalations between spherulite and shrub levels, displaying sharp or gradational contacts, and irregular to plane-parallel laminations. Common to rare vuggy pores.
		MUD Mudstone	Milimetric to centimetric layers of dark brown to white layers of mud due to variable degrees of calcite and dolomite replacement. Incipient irregular or plane-parallel lamination, sometimes deformed or displaced by silica. Matrix dissolution and fracture related pores are rare.

Figure 3. Summary of the main *in situ* lithotypes of the analyzed well cores according to the classification of De Ros and Oliveira [34].

Reworked		CCA Calcarenite	Intraclasts of calcite aggregates, mud and chert. Massive or locally showing plane-parallel lamination, medium- to coarse-grained, composed of sub-rounded to rounded particles and moderately to poorly sorted. Interparticle and vuggy pores are common.
		RCA Rudaceous Calcarenite	Calcite aggregate intraclasts, massive or locally showing irregular lamination, moderately to poorly sorted, very coarse-grained rounded particles. Interparticle pores are common and vuggy pores are rare.
		CRD Calcirudite	Calcite aggregate intraclasts, massive or locally with incipient irregular lamination, poorly sorted, very coarse- to pebble-sized, with angular to rounded particles. Vuggy and interparticle pores are common to rare.

Figure 4. Summary of the main reworked lithotypes of the analyzed well cores according to the classification of De Ros and Oliveira [34].

Table 1. Summary of the main lithotypes described in each well according to the classification of De Ros and Oliveira [34].

A	Predominance of in situ rocks (max. 6.25 m) with rare intercalations of reworked deposits (max. 68 cm). In situ rocks consist predominantly of shrub-spherulstone (max. 2.9 m) and muddy spherulstones (max. 1.4 m). Silicification is concentrated at the base and top of the core.
B1	Predominance of in situ rocks (max. 8.8 m) with intercalated reworked deposits at the top and in situ rocks at the base of the cored interval. In situ rocks predominantly consist of shrubstones (max. 3.7 m), muddy shrubstones (max. 2 m), and cycles of muddy shrubstones and muddy spherulstones with high frequency, centimetric intercalations. Reworked rocks are mostly composed of calcarenites (max. 4.53 m) and rudaceous calcarenites (max. 3.2 m). Silicification is restricted to the top and the base of the core.
C1	Predominance of reworked deposits (2.18 m) with thick in situ intercalations (max. 3.12 m) at the top, transitioning to in situ predominance (max. 17.54 m) towards the bottom of the core. In situ rocks consist predominantly of muddy spherulstones (max. 2.6 m), shrubstones (max. 2.6 m), and shrub-spherulstones (max. 1.7 m). Reworked deposits are represented by mostly calcarenites (max. 2.18 m) and rudaceous calcarenites (max. 1.7 m). Silicification is dispersed throughout the core.

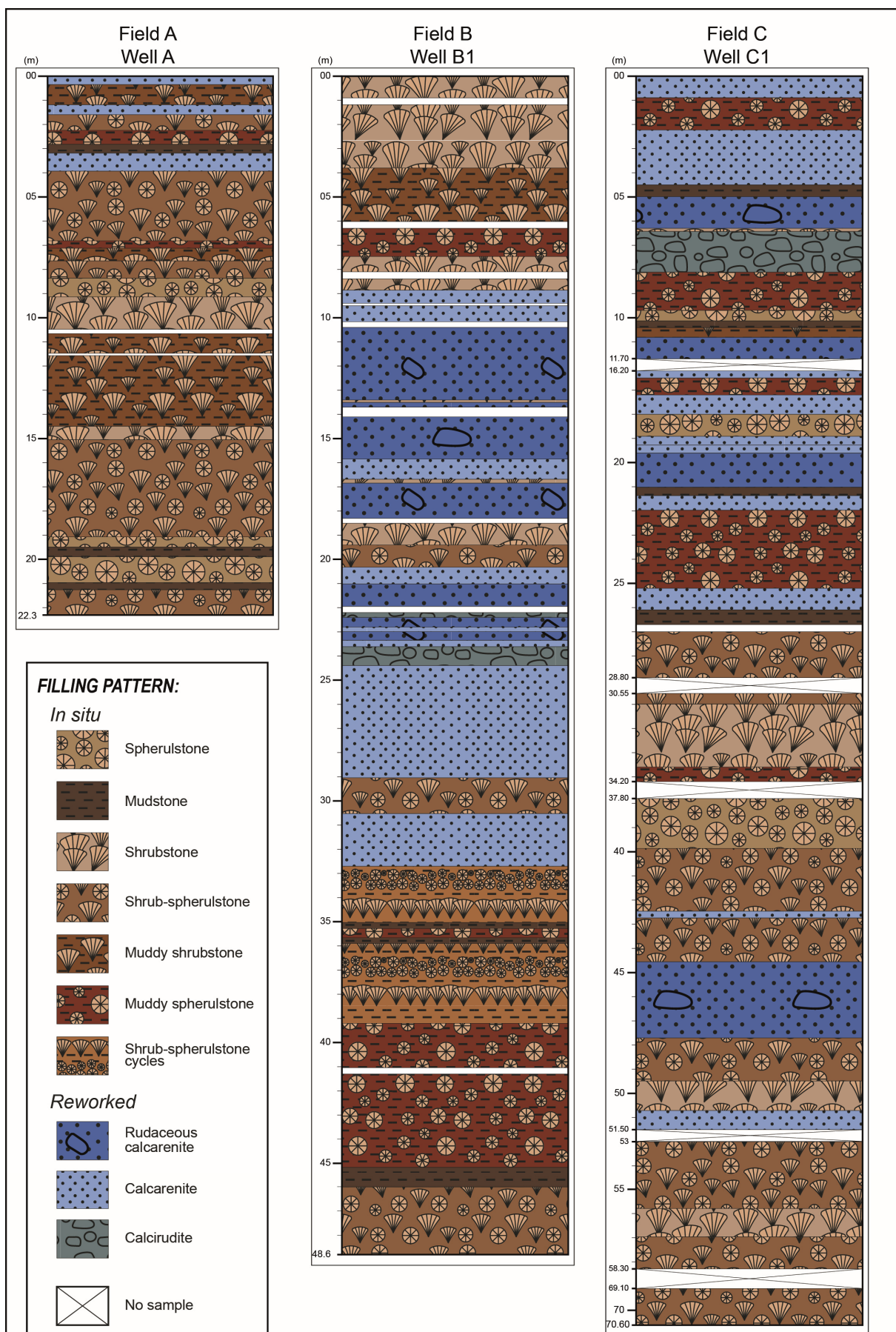


Figure 5. Summary of the distribution of lithotypes in each studied well core.

5. Petrological Characteristics of the In Situ Deposits

The BVF in situ deposits are composed of calcite spherulites and shrubs and the Mg-clay matrix, corresponding predominantly to muddy spherulstones and muddy shrubstones, followed by rare shrubstones, shrub-spherulstones, and mudstones (*sensu* De Ros and Oliveira [34]). Spherulstones are extremely rare, only represented by two samples. Muddy shrubstones and shrubstones tend to be more common toward the top of the wells, though they also occur as millimetric to centimetric intercalations with muddy spherulstones and as centimetric layers between reworked intervals.

Muddy spherulstones display well-developed lamination related to the concentration of spherulites (Figure 6A), detrital materials, and peloids. Muddy shrubstones, shrub-spherulstones, and shrubstones display poorly defined laminations caused by the concentration of the carbonate aggregates, as well as detrital material, and clay peloids. The differential dolomitization of certain layers, particularly those with abundant detrital materials emphasized these laminations (Figure 6B). The lateral coalescence of calcite shrubs and/or spherulites also highlighted the horizontal laminations. Samples formed by coalesced shrubs (shrubstones *sensu* De Ros and Oliveira [34]; Figure 6C), especially those originally devoid of the Mg-clay matrix (*i.e.*, syngenetic shrubstones), form a crystalline framework that is distinct from other in situ samples.

5.1. Constituents and Their Paragenetic Relationships

5.1.1. Magnesian Clay Minerals

Magnesian clay minerals are one of the main components of the in situ rocks, predominantly occurring as a laminated matrix with original strong parallel orientation replaced and displaced by the calcite aggregates (Figure 6A) and locally occurring as clay peloids (Figure 6D). In some samples, the matrix shows a dark brown hue, related to disseminated amorphous organic matter (Figure 6A). The matrix displays high luminescence under EPI analysis and is completely dull under CL.

The size of clay peloids varies significantly, from 0.04 to 0.5 mm, with the smaller particles predominant in mud-rich rocks and the coarser particles commonly found in shrubstones lacking a laminated matrix. Fine-grained peloids commonly display stronger diagenetic alteration than the laminated matrix, replaced by cryptocrystalline silica, microcrystalline calcite and dolomite, and pyrite. Peloidal laminae are preferentially replaced by spherulites, shrubs, and dolomites. A clay pseudomatrix was locally formed from the compaction of peloids. Locally, peloids were covered by mostly continuous clay coatings (Figure 6D) and were elsewhere identified as neoformed sepiolite [40]. The laminated matrix was locally transformed into fibrous clay with a cross-cutting orientation (Figure 6E). Clay coatings also locally cover matrix-replacive blocky and saddle dolomite.

Out of the 29 clay samples analyzed, 25 samples displayed a 15 Å peak, which expanded to 17 Å with ethylene glycol, characteristic of smectites. After heating at 550 °C, all samples collapsed to 9 Å, and with glycerol solvation, sixteen samples displayed a return of the 17 Å peak. Utilizing the Christidis and Koutsopoulou [39] criterion, the nine samples which did not re-expand were identified as stevensite, and the sixteen samples which showed re-expansion were identified as saponite/hectorite. Four samples showed kerolite, always associated with smectitic clays. Seven samples displayed a broad reflection with an asymmetric leftward shoulder at 10 Å associated with the characteristic smectite peak, which was interpreted as stevensite–kerolite mixed layers. Diffractograms of samples with the characteristic interpreted signals can be found in Supplementary Materials.

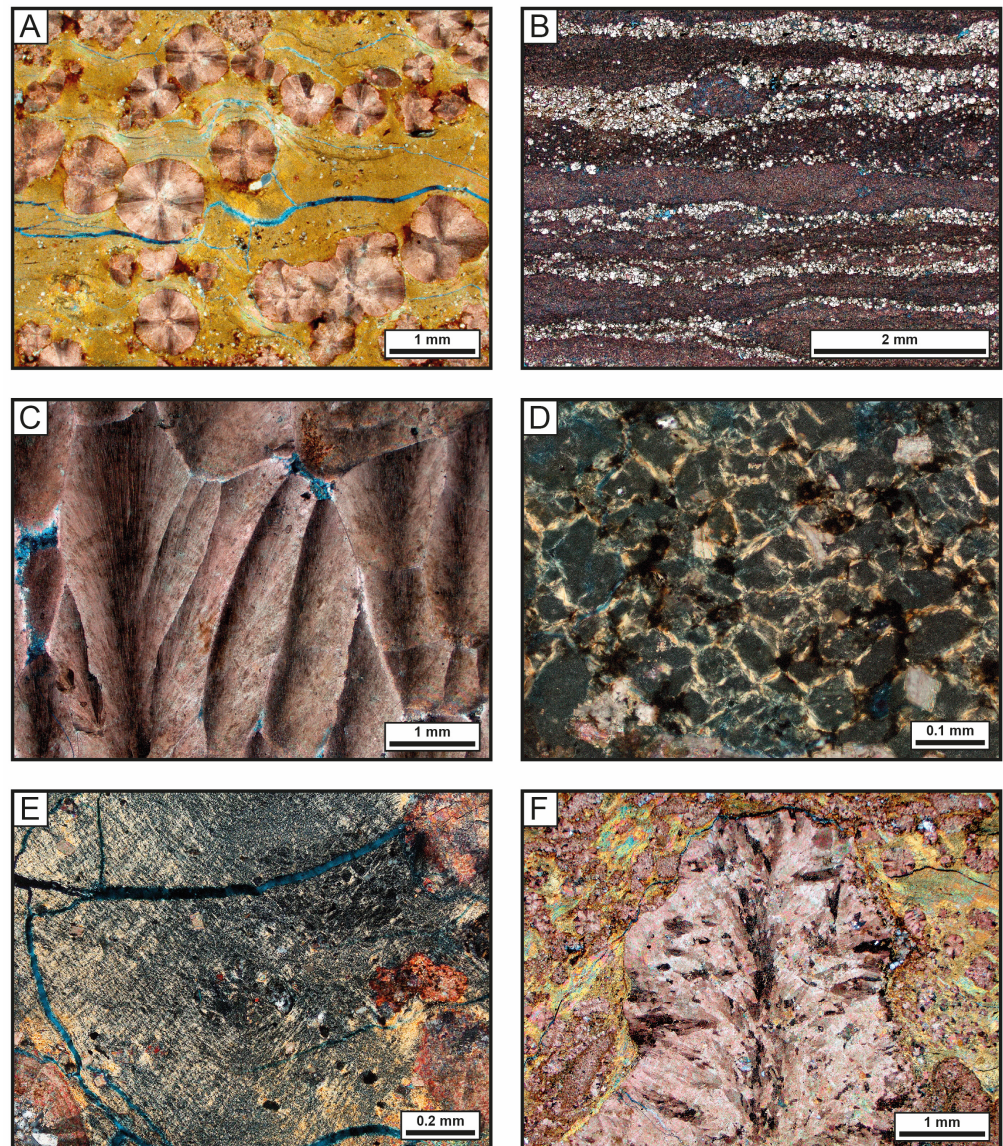


Figure 6. Main petrographic components observed in the studied wells. (A) Muddy spherulstone with calcite (stained pink) spherulites replacing and displacing organic-rich laminated Mg-clay matrix (uncrossed polarizers, //P). (B) Microcrystalline calcite and blocky dolomite intensely replacing original matrix laminations (crossed polarizers, XP). (C) Coalesced shrubs with preserved original texture and without clay matrix (XP). (D) Clay peloids covered by clay coatings (XP). (E) Transformed Mg-clay matrix showing chaotic to cross-cutting texture (XP). (F) Calcite shrub replacing and displacing laminated matrix, with recrystallization following the original internal texture (XP).

5.1.2. Calcite

Low-Mg calcite is the main mineral of the in situ rocks, occurring mostly as spherulites and shrubs. The spherulites (0.2 to 0.6 mm in diameter) are fibrous-radial aggregates that replaced and displaced the clay matrix (Figure 6A), locally displaying clay peloid nuclei, which are usually replaced by microcrystalline calcites. Shrubs are fan-like or plumose fibrous calcite aggregates (fascicular–optic sensu Kendall [41] or simply fascicular) with a sweeping extinction pattern (Figure 6C,F). They may be longer than 2 mm but are, on average, 0.5 mm long. Shrubs either replaced and displaced the clay matrix (Figure 6F) or covered and encrusted previously formed shrubs, clay matrices, and peloids (Figure 6C). Intermediate forms between spherulites and shrubs are represented by asymmetric and lobate spherulites.

The recrystallization of spherulites and shrubs is very common, presenting several patterns. Spherulites are usually recrystallized to triangular sectors following the original radial structure, though they may also display macro- to microcrystalline calcite mosaics without preferential orientation. Shrubs are less recrystallized than spherulites, usually forming sectors that follow their internal structure, partially preserving their sweeping extinction pattern (Figure 6F). Both spherulites and shrubs engulfed detrital grains and clay peloids (Figure 7A). Peloids are locally concentrated in bands along the growth structure of shrubs, where they may be partially or completely dissolved or replaced by calcite partially following aggregate orientation (Figure 7B).

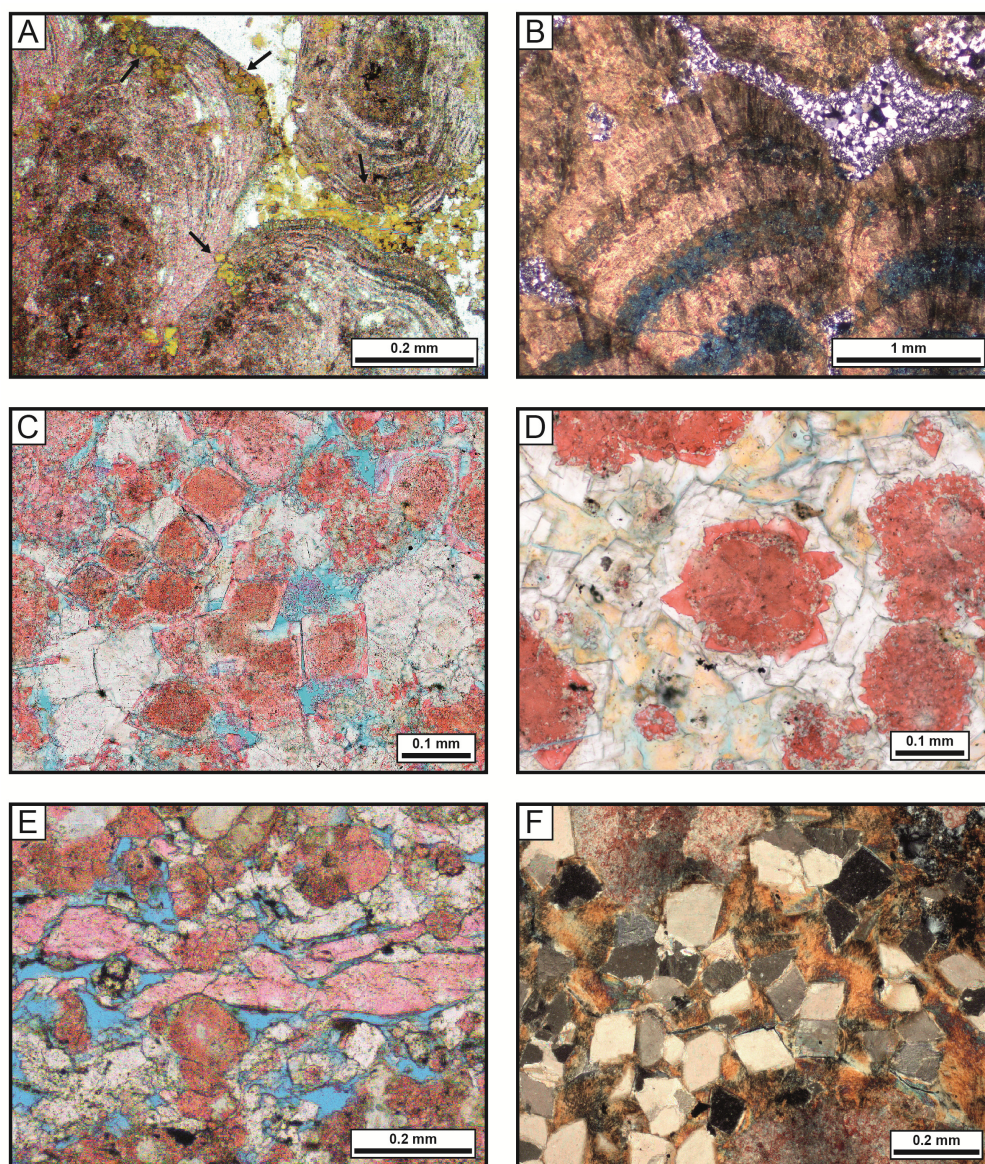


Figure 7. Main eodiagenetic components in the studied samples. (A) Peloids engulfed and partially replaced by calcite shrubs (arrows; //P). (B) Shrubs with dissolution along growth lines, with replaced peloid remnants (XP). (C) Blocky calcite crystals with rounded inclusions-rich nuclei and blocky to saddle dolomite cement (not-stained) (//P). (D) Blocky calcite rims around spherulites, covered by blocky dolomite rims that replaced the matrix (//P). (E) Lamellar calcite and dolomite in muddy spherulstone with pervasive matrix dissolution (//P). (F) Rhombohedral dolomite replacing Mg-clay matrix (XP).

Other forms of calcite possess blocky, macrocrystalline, and microcrystalline habits. Blocky calcite occurs by directly replacing the matrix, similarly to dolomite, locally with rounded inclusion-rich nuclei (Figure 7C); replacing matrix as rims covering the calcite shrubs and spherulites; or lining dissolution, inter-aggregate, and fracture pores (Figure 7D). The microcrystalline calcite usually replaced the matrix, especially in levels with detrital grains or clay peloids, commonly intercalated with levels replaced by microcrystalline to blocky dolomite (Figure 6B). Such calcite layers and lenses vary significantly in thickness, from 0.05 to 1 mm, the thicker displaying remnants of small (<0.1 mm) calcite spherulites. Macrocrystalline calcite-cemented fractures and pores from the dissolution of aggregates and the matrix and locally replaced the matrix. Rare lamellar aggregates of calcite crystals perpendicular to the lamination-filled matrix shrinkage pores together with lamellar dolomite/magnesite and replaced the matrix (Figure 7E).

Spherulites show mostly homogenous orange luminescence under CL. Shrubs show a distinct zonation pattern under CL, with predominantly dull red luminescence cut by bright orange bands following shrub growth patterns.

5.1.3. Dolomite

Dolomite is an important diagenetic component in the BVF, occurring mostly as blocky (Figure 7F), saddle, or microcrystalline crystals replacing the Mg-clay matrix, preferentially where detrital grains are common (Figure 8A). Saddle dolomite crystals with incipient sweeping extinction are commonly mixed with well-formed, uniform-extinction rhombohedral dolomite. Blocky dolomite locally occurs as discontinuous rims around spherulites and shrubs, covering and partially replacing blocky calcite rims in some cases (Figure 7D). Some blocky dolomite crystals display rounded inclusion-rich nuclei and clear euhedral borders. Blocky dolomite commonly displays a bright red luminescent core, followed by an orange zone bordered by a dull red edge in CL. UV fluorescence displays a similar pattern (Figure 8B) or a dull yellow luminescence. Saddle dolomite commonly filled fractures and pores from extensive matrix dissolution and also locally replaced the original matrix (Figure 8C). Saddle dolomite is largely non-fluorescent under UV and CL, locally with bright cores and small alternating bright bands towards the edges. Microcrystalline, blocky, and saddle dolomite also replaced calcite spherulites and shrubs, though significantly less than the Mg-clay matrix. Dolomite rarely replaced the spherulitic and fascicular calcite pseudomorphically.

5.1.4. Other Carbonates and Minor Diagenetic Constituents

Lamellar aggregates of dolomite or magnesite are locally important. These aggregates filled pores generated by the shrinkage of the laminated Mg-clay matrix and were locally covered by rims of the same carbonates [24] (Figure 8D). The lamellar aggregates follow matrix laminations previously deformed by the precipitation of the spherulites, consequently forming wavy bridges among them. Locally, the lamellar aggregates are floating within pores formed by the complete dissolution of the host matrix [21] and partially broken by compaction. The UV fluorescence pattern of the lamellar carbonates displays dull centers followed by brighter zones (Figure 8E), as shown by Carramal et al. [24]. Rare prismatic, fibro-radial, and acicular crystals of dawsonite ($\text{NaAlCO}_3(\text{OH})_2$) locally fill matrix dissolution and aggregate fracture pores (Figure 8F). Pyrite is common but not volumetrically significant, usually as microcrystalline or framboidal crystals replacing clay peloids, matrix, carbonate particles, and calcite aggregates. Pyrite is concentrated in detrital-rich layers and along stylolites. Macrocrystalline quartz occurs by filling aggregate fractures, vugular, matrix, and aggregate dissolution pores. Microcrystalline quartz occurs mostly as a matrix replacement. Prismatic quartz and fibrous radial chalcedony occur as cements that fill vugular and matrix dissolution pores. Spherulitic and hemispherulitic chalcedony are rare and replace the matrix. Cryptocrystalline silica locally replaces the matrix.

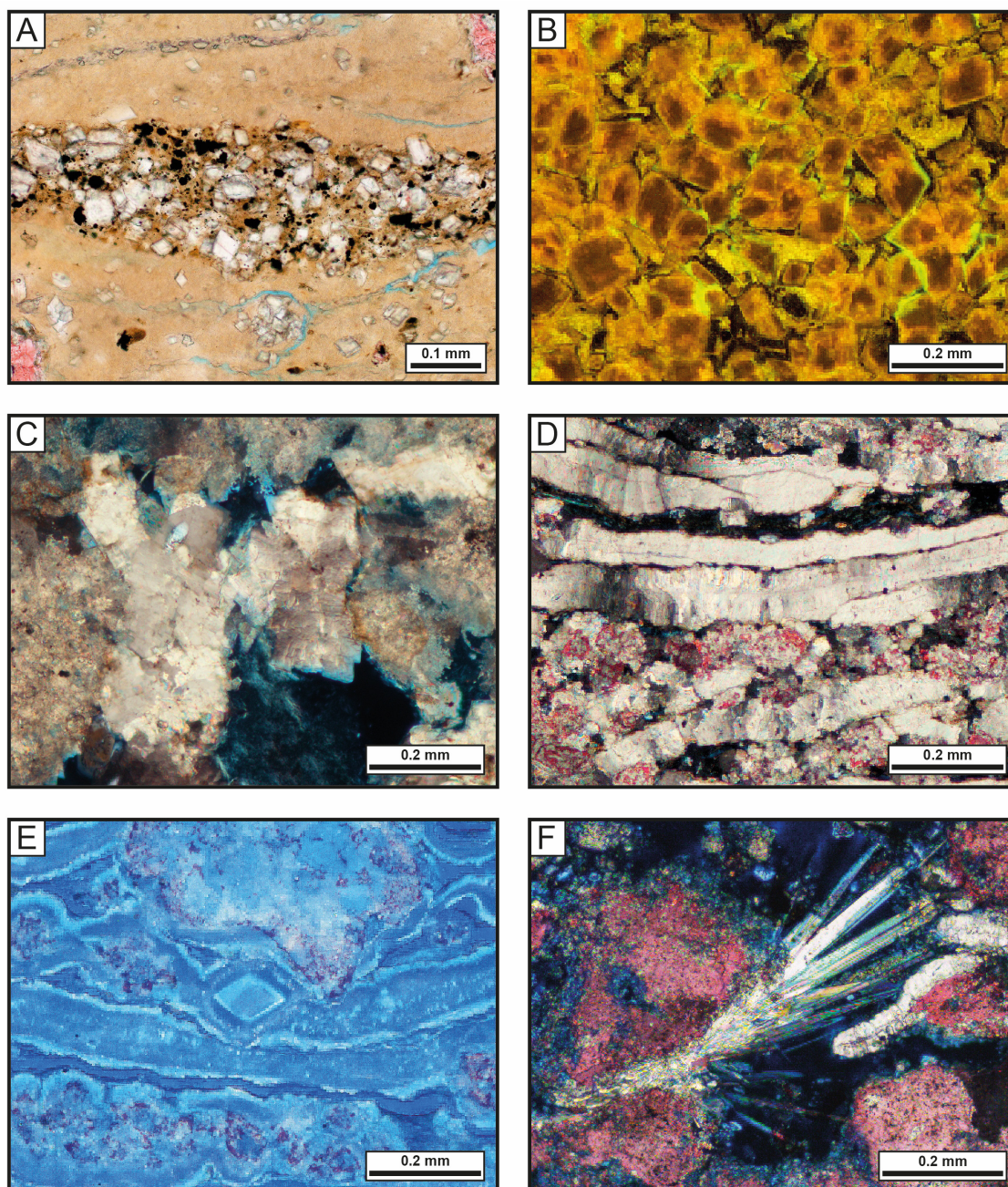


Figure 8. Main eodiagenetic and late-stage components in the analyzed samples. (A) Microcrystalline and blocky dolomite preferentially replacing level with detrital material and organic matter concentration (black grains). (//P). (B) Matrix-replacive blocky dolomite with dull brown core followed by orange zone, locally with bright green and completely dull cores (UV Epifluorescence; UVF). (C) Saddle dolomite replacing partially dissolved matrix. (XP). (D) Lamellar carbonate replacing matrix remnants covered by perpendicular palisade crystals filling matrix shrinkage pores. (XP). (E) Blocky dolomite with dull rounded core and bright edge, and lamellar carbonate with a dull core followed by brighter perpendicular fibrous and a very bright edge (UVF). (F) Acicular dawsonite in matrix-dissolution pores. (XP).

5.1.5. Detrital and Intrabasinal Grains

Intraclasts of eroded and redeposited spherulites and fragments of shrubs and other calcite aggregates occur as layers intercalated between the in situ deposits. Superficial ooids with intraclastic nuclei and originally clay envelopes abraded and replaced or filled by fibrous to microcrystalline calcite and dolomite also occur in these layers but not in the

in situ rocks. Rare articulated and disarticulated ostracod and phosphatic bioclasts were partially engulfed by calcite shrubs and spherulites. Detrital grains correspond mostly to silt to very fine sand grains of quartz, feldspar, and micas; rare celadonite and heavy minerals occur mixed with the Mg-clay matrix, commonly concentrated in some laminae or engulfed by the calcite aggregates.

5.1.6. Pore Types

The main pore types in the in situ rocks are secondary inter-aggregate pores that resulted from widespread matrix dissolution (Figure 8E) in muddy spherulstones (Figure 7E), muddy shrubstones, shrub-spherulstones, and primary inter-aggregate pores in syngenetic shrubstones (Figure 6C). Other important pores are intra-aggregate, from the partial dissolution of calcite spherulites and shrubs and of included clay peloids, usually along shrub growth lines in muddy shrubstones and shrubstones (Figure 7B). Aggregate fracture pores are more common in shrubs, rare in spherulites, and predominantly found in matrix-free shrubstones and muddy shrubstones. The nuclei of blocky calcite and dolomite are locally dissolved. Matrix shrinkage pores are common in muddy spherulstones (Figures 6A and 8C,D) and rare in muddy shrubstones but volumetrically of little significance in most cases. Vuggy pores (Figure 8F) are common in extremely altered samples of any class but slightly more common in muddy shrubstones.

6. Discussion

6.1. Genesis of the Pre-Salt Minerals

The conditions of the formation and evolution of the Pre-salt deposits are still poorly understood, yet some constraints are established. Tutolo and Tosca [14] and Pozo and Calvo [42] indicated that Mg-clay minerals are stable in high pH conditions, with variable salinities. Tutolo and Tosca [14] established that, under high silica concentrations and alkaline lakes buffered at $\text{pH} > 10$, the precipitation of spherulitic calcite would be favored. Shrub formation has been attributed to higher HCO_3^- concentrations than spherulites. This may be promoted by evaporation, CO_2 degassing, and/or increased CO_2 supply from groundwater [16,20,25,43,44]. The absences of syngenetic sulfates and chlorides in Pre-salt strata indicate low SO_4^{2-} and Cl^- concentrations, thus indicating the absence of seawater influence [14,25]. The sources for the large volumes of Mg^{2+} , Ca^{2+} , silica, and CO_2 required for the massive formation of Mg-clays and carbonates in the Pre-salt, however, are still not revealed. Several authors suggested an origin derived from a mixture of different sources, including the granitic–gneissic basement rocks, rift and Aptian magmatism, the rift deposits, and the exhumation and serpentinization of the upper mantle [13,14,19].

Considering the formation and evolution of the BVF system, characterized by complex diagenetic intensity and distribution patterns, as well as high-frequency intercalations of depositional and diagenetic processes, the interactions among carbonates and Mg-clays will be discussed according to their genetic processes and timing, under syngenetic, eodiagenetic, and mesodiagenetic/hydrothermal conditions.

The syngenetic processes by Chilingar et al. [45] refer to any product formed simultaneously or penecontemporaneously to deposition on or above the water–sediment surface. Eodiagenesis refers to processes and products generated after the deposition still under the influence of depositional waters and low P and T conditions [46,47]. Mesodiagenesis refers to those processes and products generated under effective burial and the influence of considerably modified fluids, higher P and T [46–48]. Hydrothermal processes, however, are somewhat harder to define. Machel and Lonnee [49] discussed that the term can only be properly used where the formation temperature of a mineral is higher ($>10^\circ\text{C}$) than that of the host rock. However, as Lima and De Ros [16] argued, this constraint is rather impractical and difficult to determine. These authors instead broadened the hydrothermal definition to any mineral assemblage that is related to the focusing of hot fluid flow through faults or fracture systems, commonly but not exclusively related directly or indirectly to magmatic processes.

6.2. Syngenetic Interactions

Syngenetic interactions in the BVF involved those developed between Mg-silicates (stevensite, kerolite, stevensite–kerolite mixed layers, saponite, and sepiolite [24,50–52]) formed in the lake water column (homogeneous nucleation) or on the surface of pre-existing solids (heterogeneous nucleation as on ooids), and fascicular calcite shrubs precipitated on the sediment–water interface (Figure 9). Such magnesian clays constitute the depositional background of Pre-salt deposits and the laminated or peloidal matrix of most in situ rocks. The only notable exceptions are matrix-free shrubstones formed above the sediment–water interface, which are, nevertheless, usually associated with Mg-clay peloids (Figure 9B).

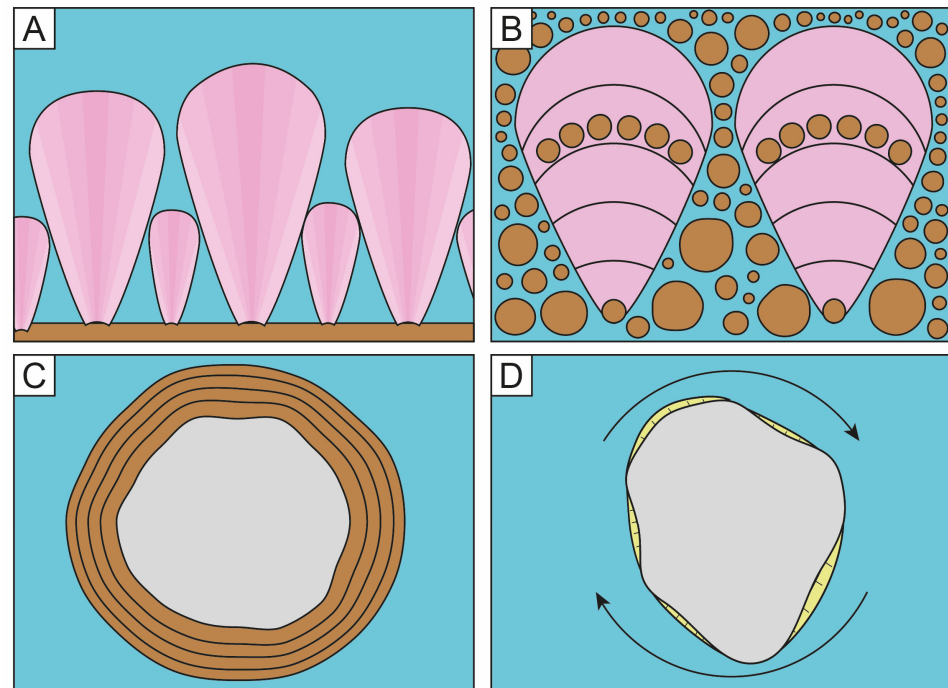
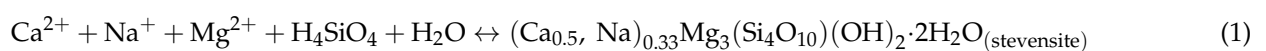


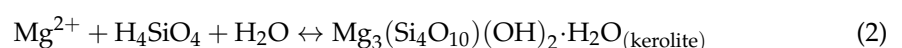
Figure 9. Schematic representation of the main syngenetic relations between carbonates and clays. (A) Syngenetic calcite shrubs growing over a matrix substrate. (B) Syngenetic calcite shrubs engulfing peloids according to their growth lines. (C) Clay ooid formed over a carbonate intraclast. (D) Reworked clay ooid with envelopes replaced by carbonate and abraded.

Pre-salt shrubs were formed either on the sediment–water interface (syngenetic) or just below it, within the Mg-silicate matrix (eodiagenetic; [16,17,24]). They are texturally similar to the Archean and Proterozoic crystalline stromatolites or “sea-floor cements” [53–57], Phanerozoic crisis horizons [56,58,59], and crystalline travertines [43,60] (Figure 6C,F). All these deposits are considered as being the result of abiotic precipitation, as interpreted for the Pre-salt shrubs (e.g., [8–10,16,17,20,25,56,58,59,61]). Gomes et al. [17] interpreted the predominantly vertical orientation of the shrubs as being the result of higher precipitation rates and ion supply via advection.

Al-free magnesian clay minerals are formed from fluids highly concentrated in Mg^{2+} and silica, with specific mineral species resulting from a combination of Mg/Si ratios, salinity, and pH [42,62]. Stevensite requires $pH > 9$ and high salinity with variable Mg/Si, while kerolite forms in lower salinity conditions with $pH > 9$ or under high salinities with $pH < 9$ [42], according to Equations (1) and (2).



or



Tutolo and Tosca [14] interpreted the association of these clays with spherulites and shrubs to indicate high pH (~10–10.5) with high concentrations of silica and alkali cations, such as Na^+ and Ca^{2+} . Wright and Tosca [9] considered the large-scale deposition of the laminated matrix as a result of the settling and crystallization of a colloidal gel formed while suspended in the water column. Conversely, Carramal et al. [24] argued that, according to Stoke's law, the settling of gels would require a long time under very quiet conditions, which is incompatible with the large-scale and recurrent Mg-clay deposition seen in the Pre-salt, frequently associated with siliciclastic silt. Furthermore, the authors also indicated that well-laminated clay matrix fabrics would not be formed from the crystallization of an amorphous gel, which would result in chaotic orientation, as seen, for instance, in the crystallization of opal (cf. French et al. [63] and French and Worden [64]). They also argued that the deformation of the matrix laminations by the very early spherulites and shrubs would indicate that the Mg-clays were already deposited with a laminated and strongly oriented fabric. Consequently, Carramal et al. [24] indicated that the matrix was deposited as clay particles instead of the Mg-Si gel, as suggested by Wright and Barnett [8].

Mg-clay peloids may have formed through the complete replacement of pre-existing particles, from the reworking of matrix or other clay grains (such as ooids and intraclasts), or from clay flocculation while in suspension. The first case is common in volcanic settings, with alteration providing ions and creating alkaline environments that favor clay formation [65,66]. Furthermore, the formation of "green clays", such as berthierine and glauconite, is known to form peloids through the infilling and replacement of fecal pellets, carbonate bioclasts, and various detritals [67,68]. The second case is better represented by glauconite grains, which are commonly reworked, possibly transported, and incorporated into penecontemporaneous or younger sediments, termed para-autochthonous and allochthonous [69,70]. In addition, Armelenti et al. [71] described the widespread gravitational redeposition of previously formed stevensitic peloids and ooids in the rift section of the Campos Basin. In the third case, clay flocculation is a result of the complex interactions between clay minerals suspended in saline fluids, which are attached in progressively larger particles, increasing their settling velocity [72–76]. Some degree of turbulence is needed to maintain clay particles in suspension for peloid development, requiring a moderate amount of energy in the system [77,78].

Clay peloids are quite common in the in situ rocks of the Pre-salt, yet very few studies have focused on them (e.g., [24]). Though not as ubiquitous as the laminated clays, clay peloids are quite common and significant in constraining environmental conditions. Their occurrence can be recognized as follows: (1) in laminae mixed with detrital materials; (2) among matrix-free shrubstones (Figure 6C); and (3) engulfed in eodiagenetic (Figure 7A) and syngenetic shrubs and eodiagenetic spherulites. As volcanoclastic materials are scarce throughout the Barra Velha Fm., restricted mostly to areas close to the Cabiúnas Fm., the Pre-salt peloids were most likely formed through reworking and/or flocculation. The common presence of small clay peloids associated with siliciclastic grains suggests that they are related to an increased sediment supply associated with energy increase in the system, pointing to a resedimented origin for these particles. These layers are often highly modified by diagenesis, usually in the form of calcite and dolomite replacement, as discussed in the next section (eodiagenetic).

The lack of a laminated clay matrix within shrubstones indicates that shrub precipitation occurred during periods of decreased clay deposition. Whether this is the result of unfavorable changes in the lake chemistry and pH for Mg-clay authigenesis [8] or the increase in the wave or bottom current energy impeding clay-sized particle deposition [16,24] remains unclear. However, peloids are quite commonly engulfed by syngenetic shrubs, indicating peloid deposition during shrub formation and the persistence of clay deposition during calcite precipitation. The alternation of growth zones with abundant engulfed peloids and "clean" layers within shrubs seems to further indicate that calcite and clay deposition were concomitant during some periods of lake evolution (Figure 10). The zones with no engulfed peloids may be related to increased wave or current energy in the system

related to the deposition of larger peloids. Wright [25] suggested that restricted and shallow lakes are highly dynamic systems, with meter-scale water-level fluctuations occurring throughout decades as a result of environmental and hydrodynamic changes. However, such fluctuations could not explain the high-frequency intercalations in the composition and energy observed in the Pre-salt deposits. This is because fluctuations in rainfall, run-off and groundwater discharge, evaporation rates, and connection to other water bodies could not change the chemistry and the level of the huge lacustrine system as reflected in the high-frequency intercalations observed in the deposits.

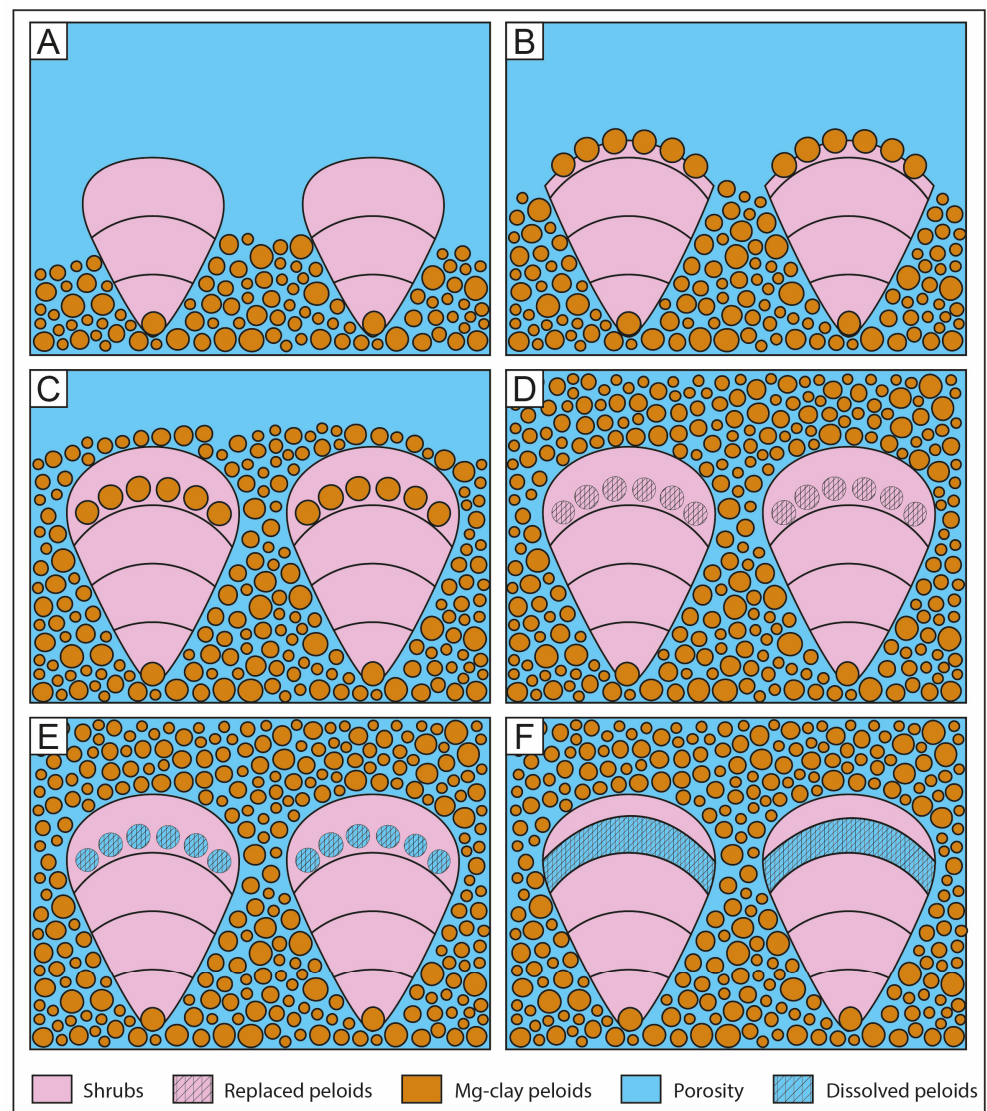


Figure 10. Schematic representation of dissolution of shrubs following their growth lines. (A) Initial stage of shrub formation with clay peloids as substrate. (B) Peloids deposited over shrubs and incipiently engulfed by the shrubs. (C) Shrub growth continues, engulfing the peloids. (D) Engulfed peloids replaced by calcite, leaving “ghosts” of their shapes. (E) Engulfed peloids dissolved. (F) Dissolution follows previously formed pores to create dissolution zones in the shrubs.

Some authors suggested that the Pre-salt Mg-silicates may have nucleated on or within EPS (extracellular polymeric substances generated by microbial activity [11,12]). Indeed, some papers reported on Mg-Si gels formed within EPS of microbial mats and thrombolites [79–82]. This relates to the trapping of ions such as Mg, Si, and Ca by EPS under highly alkaline conditions [79–83]. Tosca and Wright [62] argued that the hypothesis of a microbial substrate would restrict Mg-silicate occurrence to specific microbial facies,

which is not observed in the Pre-salt deposits. Carramal et al. [24] have also raised important objections against the microbial model, mainly considering the sheer volume and wide distribution of Mg-silicates spanning several basins, both in the African and Brazilian conjugate margins, and the characteristics of associated carbonates that are incompatible with a microbial origin.

Carramal et al. [24] described ooids with kerolite and stevensite envelopes in the Lula Field of Santos Basin as the main components of ooidal arenites or mixed with volcanic fragments in hybrid arenites. These ooids have nuclei composed of spherulitic, fascicular, and microcrystalline carbonate intraclasts, and their clay envelopes are usually strongly replaced by microcrystalline calcite, dolomite, or silica. Mg-silicate ooids had been previously identified in the rift section of the Campos and Santos Basins [71,84,85]. Carramal et al. [24] suggested that sag-section ooids originated from heterogenous nucleation on carbonate nuclei in conditions of lower energy than those interpreted for the rift-section ooids. Later reworking partially abraded the envelopes, which, together with carbonate replacement, makes the identification of these redeposited particles difficult (Figure 11).

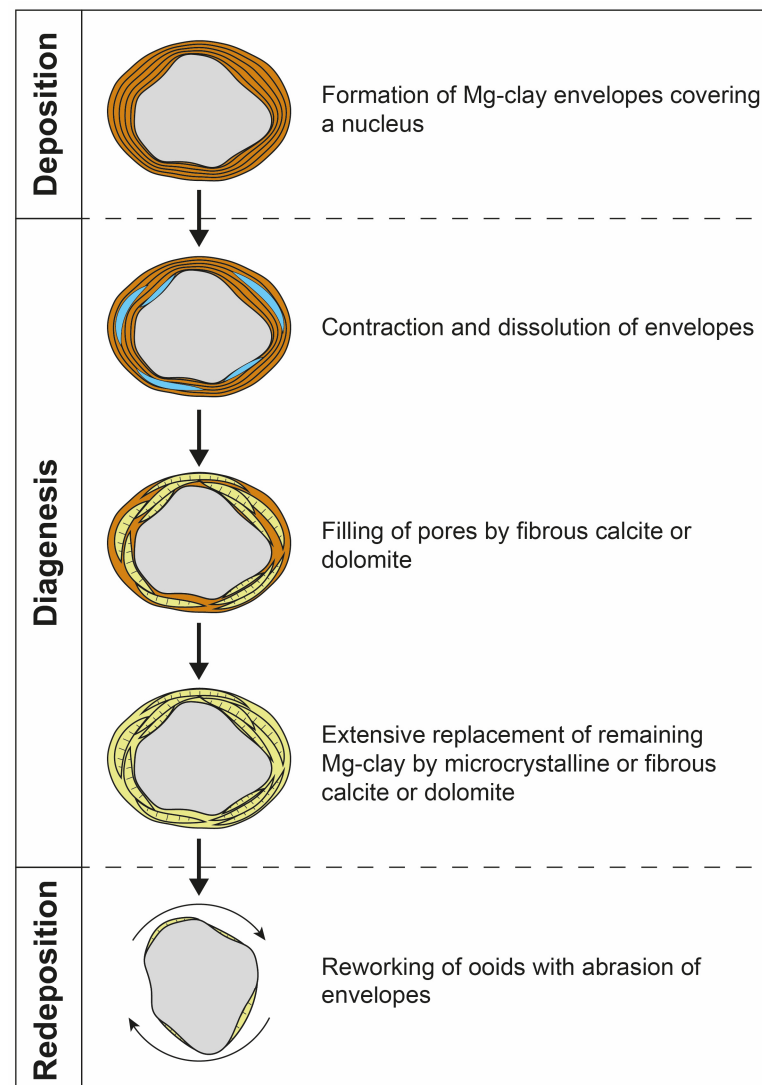


Figure 11. Schematic diagram for ooid formation, shrinkage of the clay envelopes and cementation by carbonates, complete replacement by carbonates, and later reworking and abrasion, as per Carramal et al. [24] (modified from Carramal et al. [24]).

6.3. Eodiagenetic Interactions

The eodiagenetic interactions include those developed between Mg-silicates and carbonates precipitated at very shallow burial depths beneath the sediment-water interface and still under the influence of the lacustrine waters. The spherulites and part of the fascicular shrubs replaced and deformed the Mg-clay matrix shortly after its deposition and before lithification. This is indicated by the deformation of the matrix laminations, and by remnants of the matrix included within the aggregates [8,10,16,24]. Other eodiagenetic relations include blocky calcite replacing the matrix as scattered crystals and as rims covering the calcite aggregates, matrix-replacive blocky dolomite and rims, lamellar carbonates filling shrinkage pores and replacing matrix, and matrix-replacive microcrystalline calcite (Figure 12).

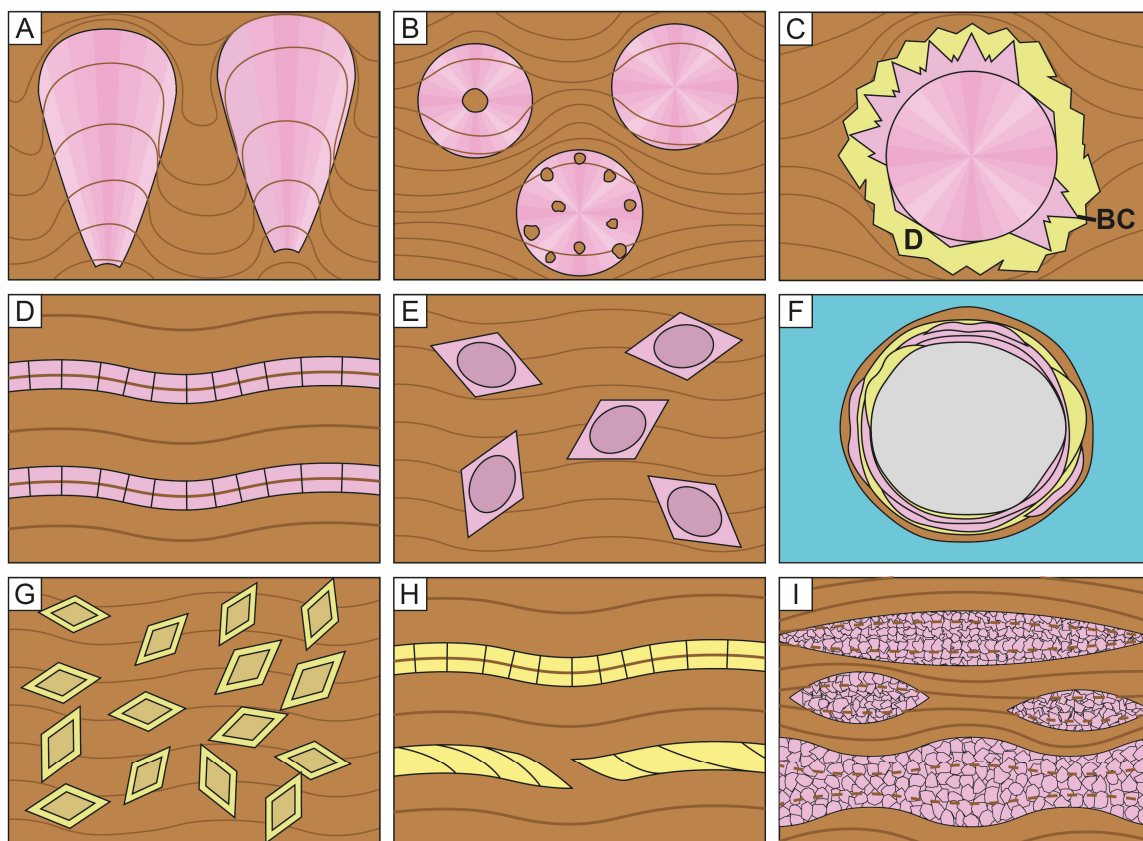


Figure 12. Schematic representation of the main eodiagenetic relations between clays and calcite (rose) and dolomite/magnesite (yellow). (A) Shrubs replacing and displacing Mg-clay matrix, deforming the original laminations. (B) Spherulites replacing and displacing Mg-clay matrix, with clay peloids serving as a nucleus and engulfed during spherulite growth. (C) Blocky calcite rims (BC) replacing matrix, formed over spherulites, and blocky dolomite rims (D) replacing matrix and covering calcite rims. (D) Lamellar calcite replacing matrix remnants and filling matrix-shrinkage pores. (E) Blocky calcite with round, turbid, inclusion-rich nuclei replacing matrix. (F) Calcite and dolomite replacing and filling clay ooid envelopes shrinkage pores. (G) Blocky dolomite with turbid nuclei replacing original matrix. (H) Lamellar dolomite filling matrix-shrinkage pores and replacing matrix remnants. (I) Microcrystalline calcite replacing and displacing matrix forming lenses and “ribbons”.

The processes involved in the formation of the characteristic Pre-salt fascicular and spherulitic calcite aggregates are part of an ongoing debate in the literature. Some authors ascribe such formation to microbially induced or influenced mechanisms (e.g., [11,12,86,87]). Others, on the basis of the unfractionated $\delta^{13}\text{C}$ values and on the abiotic formation of similar aggregates in some stromatolites and travertines (e.g., [43,54,56]), interpret their origin as a

product of abiotic, chemical precipitation (e.g., [8,10,16,24,25,88]). Wright and Barnett [8] originally interpreted the formation of spherulites as precipitated within an amorphous Mg-Si gel. However, as previously stated, Carramal et al. [24] suggested that the Mg-clay matrix was already deposited as such, on the basis of Stoke's law, the highly parallel and organized fabric, and the matrix deformation by the very early calcite precipitation. Therefore, the Pre-salt spherulitic and fascicular aggregates were formed by the abiotic replacement, displacement, and/or incrustation of the Mg-clay matrix (Figure 12A,B and Figure 13). The lobate or asymmetric spherulites represent intermediate forms between spherulitic and fascicular aggregates. Our hypothesis is, therefore, that the formation of either spherulites or shrubs was related to the distance to the water–sediment interface. Closer or on the interface, the higher ionic supply and rate of precipitation favored a preferentially vertical crystal growth [8,16,54,89].

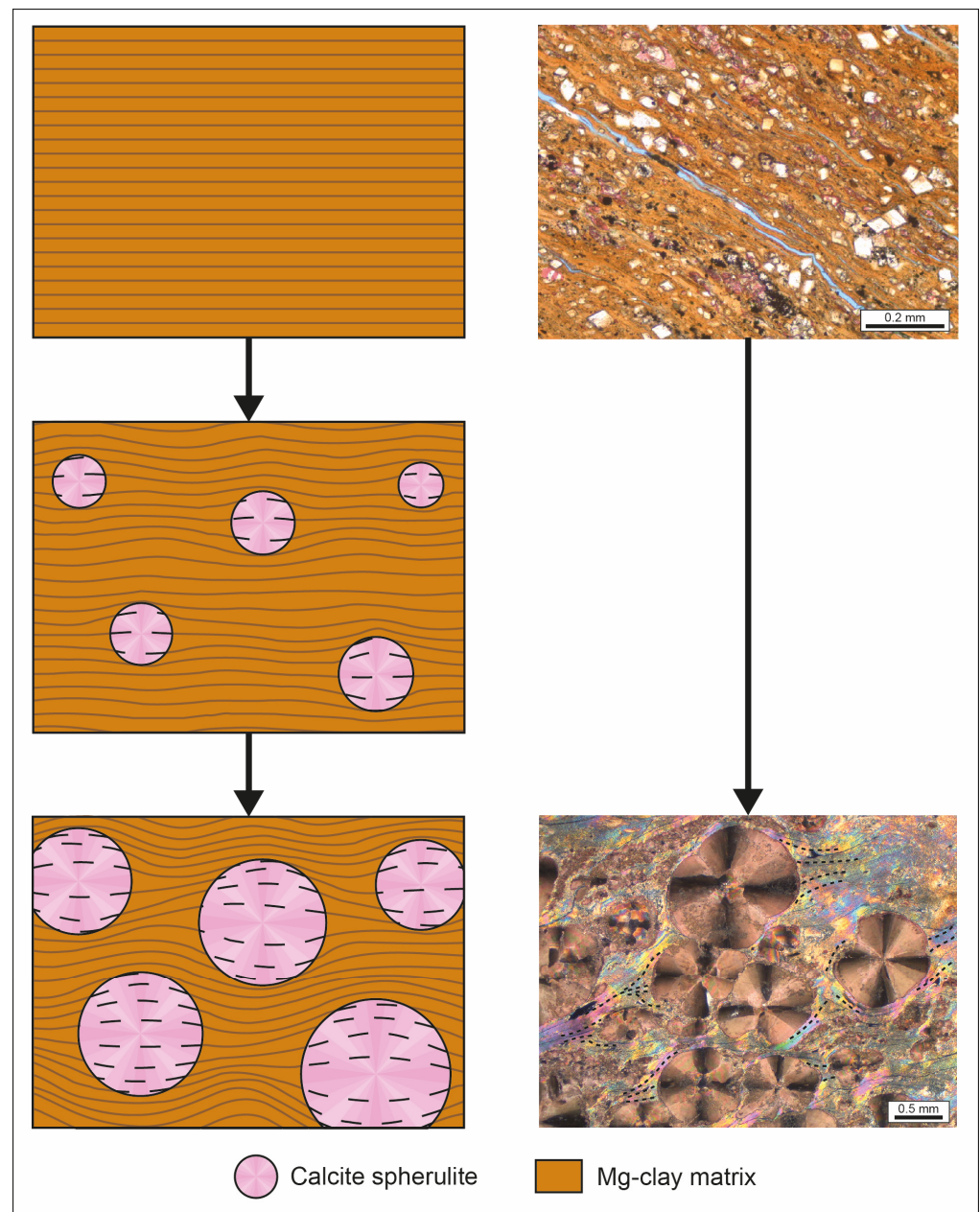


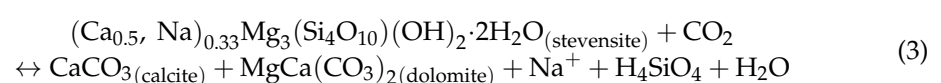
Figure 13. Schematic diagram for matrix layer deformation due to spherulite precipitation. The initial stage of parallel lamination is progressively deformed by growth of spherulites, with laminae replaced (cut) and displaced (deformed) by the aggregates.

Clay peloids and siliciclastic grains are usually found engulfed by spherulitic and fascicular aggregates (Figures 7A and 12B). This feature is found in concretions formed through the replacement and displacement of host sediment, indicative of formations under very shallow burial [90–93]. Calcite later replaced part of the engulfed peloids, generating an inclusion-rich, “turbid” texture. Rounded moldic pores within the shrubs and spherulites were formed by the dissolution of clay peloids. In shrubs which display peloids concentrated in growth zones, this dissolution porosity generated “dissolution bands” (Figure 10).

Clay coatings that formed over particles have been identified by Ramnani et al. [40] as sepiolite, suggesting that they have been formed by the partial dissolution of previous Mg-clay minerals. They further indicated that these coatings formed under eodiagenetic conditions, which agree with their continuity over the peloid surface in the studied samples. Though sepiolite may form from a precursor Mg-rich clay mineral, such as stevensite or saponite [94], it may also form directly from a solution having high Si/Mg ratios, lower salinity, and a pH of around 8–8.5 [42]. Sepiolite is also found to be associated with dolomitization processes in highly evaporative environments, covering dolomite crystals or cementing intercrystalline pores [95].

The distinction between matrix-replacive and cement phases may appear clear when the matrix is still partially preserved, but it becomes significantly harder in cases where there was complete matrix dissolution, such as in Pre-salt deposits. This can be achieved with a careful petrographic analysis of the distribution and habits of diagenetic constituents and their relation to the depositional matrix. Carbonate cement phases favor nucleation over pre-existing carbonates, occurring as rims of various habits (e.g., acicular, blocky, isopachous) or overgrowths or as pore-occluding coarse cements, frequently with drusiform coarsening towards the center of the pores. Furthermore, matrix-replacive phases typically display no preferential orientation to particle or aggregate surfaces, giving rise to the so-called ‘floating’ or random distribution [8] or are directly controlled by the existing lamination of clay minerals as the pseudomorphic lamellar phases (‘bridges’ of Wright and Barnett [8]). It is important to notice that, even though rims may form as a matrix-replacive phase, ‘floating’ crystals will not form without a previous substrate. Matrix dissolution may occur during any stage of matrix replacement and may create rocks with intercrystalline porosity among dolomite crystals, as described by Herlinger et al. [26]. Late-stage dolomite cementation may also fill any remaining porosity. A schematic summary of these characteristics is shown in Figure 14.

Tosca and Wright [62] interpreted the spherulstones without Mg-silicates as a result of a large-scale congruent dissolution of the matrix. They argued that this would be possible due to the turbostratic structure and bonding characteristics of Al-free Mg-silicates, as well as their high specific surface area. As discussed by Tosca and Masterson [96], the stability of Mg-silicates is rather limited, and small fluctuations in pH, Mg^{2+} , and silica activities may cause their dissolution. This occurs mainly due to the weak Mg–O bonds and the disordered (turbostratic) structure of the stevensite [24,97]. Tosca and Wright [62] suggested that CO_2 input would effectively decrease the pH and increase the HCO_3^- concentration, which would induce massive Mg-silicate dissolution while maintaining or even increasing carbonate stability (Equation (3)). Although conditions for Mg-silicate dissolution in the reservoirs could have easily been achieved during burial, Carramal et al. [24] reasoned that large-scale dissolution occurred during early diagenesis because the low permeability of the deposits would severely limit the development of such process under burial.



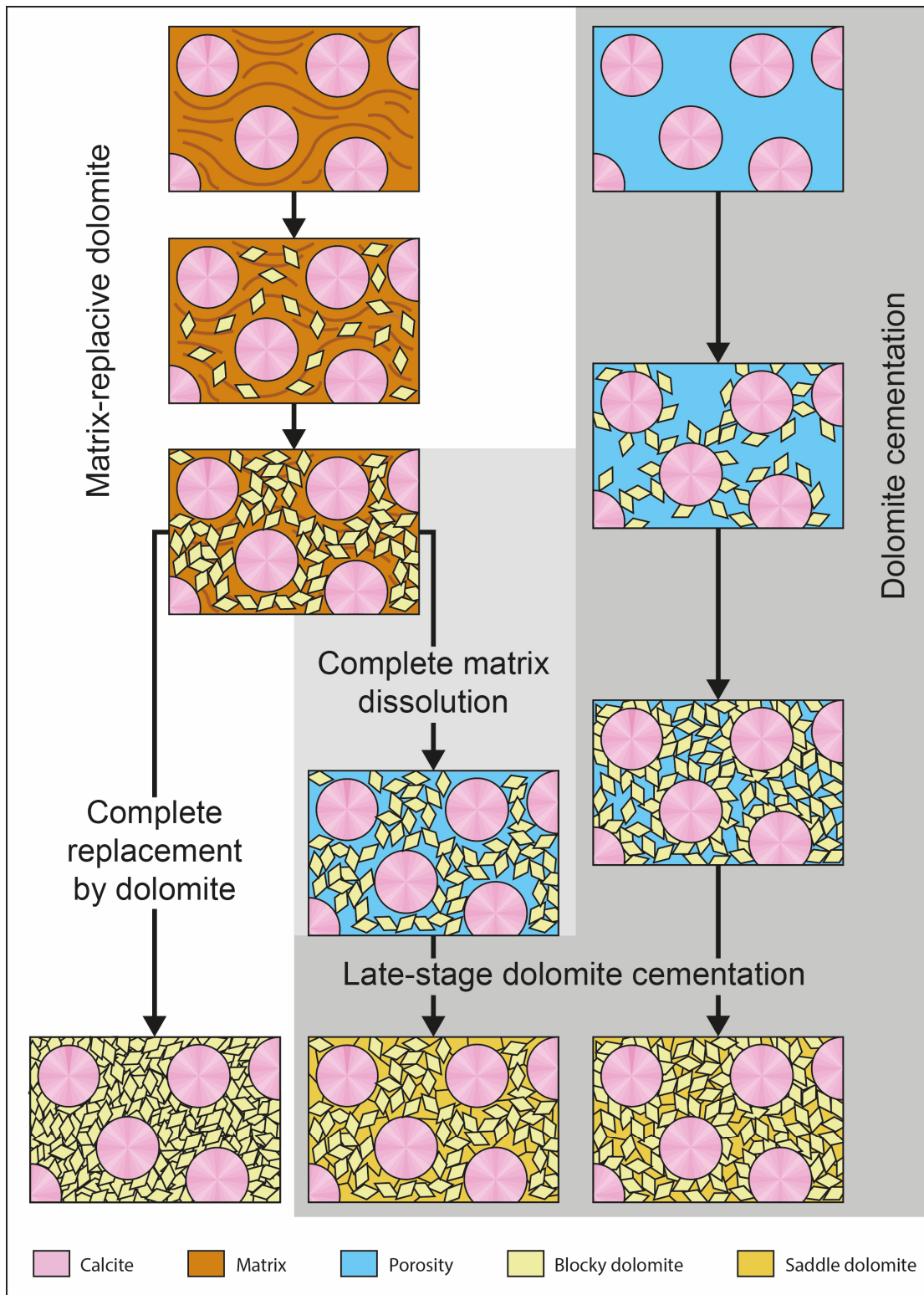
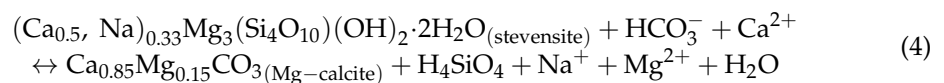


Figure 14. Schematic representation of the differential distribution generated by dolomite replacement of matrix and cementation of matrix-dissolution porosity.

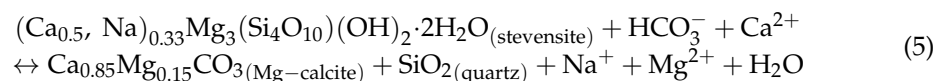
The first eodiagenetic process that followed the formation of spherulites and shrubs was the precipitation of blocky calcite rims over these aggregates, usually replacing the original matrix (Figures 7D and 12C). The habit of these rims is most likely related to the decreasing saturation of calcite in the system, favoring the precipitation of coarser

crystals over the pre-existing fibrous calcite aggregates. These rims are often found over recrystallized spherulites and shrubs, following the overall crystal orientation, indicating that calcite rims formed either during their recrystallization or shortly after.

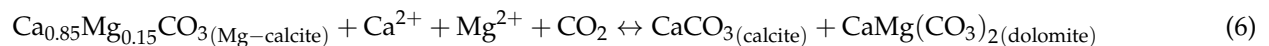
The early dolomite replacement of the Mg-clays clearly suggests that their instability favored the precipitation of dolomite [98], while calcite spherulites and shrubs are usually completely preserved. This could be explained by the relative stability of calcite due to its high HCO_3^- activity [62], which, when allied to the Mg-rich composition of the clays, would favor the precipitation of dolomite at the expense of the matrix while preserving the calcite aggregates. Conversely, the rare samples where an intense dolomitization of the aggregates occurred could represent a different original composition. Gomes [99] published XRD data showing significant volumes of still preserved high-Mg calcite (HMC) in the Santos Basin paleo-high and off-structure areas. Considering an original HMC composition for the aggregates, matrix replacement would follow Equation (4), and limited silicification of the matrix could occur due to SiO_2 being released from the clay destabilization as per Equation (5). Aggregates originally composed of HMC are more susceptible to dolomite replacement than low-Mg calcite (LMC) aggregates, usually preserving their original textures [100,101]. Therefore, the pseudomorphic dolomitization of calcite aggregates most likely took place before HMC stabilization [102]. This could also explain the varying degree of recrystallization found, where LMC would be prone to pseudomorphic recrystallization, while a late neomorphism of HMC would produce mosaic fabrics without the inheritance of the original crystalline orientation of the aggregates. Although a compelling hypothesis, direct evidence for HMC transformation to LMC (e.g., [103–105]) is still absent for the Pre-salt deposits. Although the LMC aggregates could be also generated by the neomorphism of aragonite [51], the crystalline fabric and square stepped terminations characteristic of aragonite neomorphism [106] are lacking from the Pre-salt calcite spherulites.



or



The rounded, inclusion-rich nuclei of dolomite and calcite crystals (Figure 7C) covered by euhedral overgrowths may represent a recrystallization/stabilization process of less stable phases. Proto-dolomite or HMC commonly display extremely defective forms [107], which are replaced during diagenesis to more stable dolomite or LMC calcite with euhedral or subhedral forms via a dissolution–reprecipitation mechanism, potentially resulting in the precipitation of both carbonate phases as per Equation (6) [108–111].



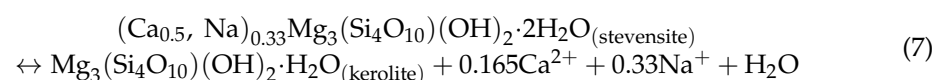
Liu et al. [112] showed experimental evidence that smectites may serve as nuclei for proto-dolomite formation under high alkalinity. Proto-dolomite is suggested to recrystallize to ordered, stoichiometric dolomite under burial [107]. An initial metastable phase is not required, however, to form the inclusion-rich “turbid” cores in blocky dolomites. These cores could represent an initial phase of matrix-replacive dolomite followed by clear overgrowths [111,113] (Figure 7D,F), suggesting at least two eodiagenetic dolomitization events for the Pre-salt. The recrystallization of earlier phases could also occur together with the overgrowths, possibly using the less stable core as an ion source for further dolomite precipitation [114–121]. Further interpretations regarding the mechanisms of dolomite precipitation in the studied areas require detailed data on dolomite cation ordering and stoichiometry.

The precipitation of lamellar dolomite or magnesite aggregates parallel to the lamination of the matrix (Figures 8C and 12H) was interpreted by Wright and Barnett [8] as a direct replacement of Mg-silicate gels or after some neoformation of clays from them

and as a product of the pseudomorphic replacement of the stevensite matrix laminations by Lima and De Ros [16]. Carramal et al. [24] identified two morphologies of lamellar dolomite/magnesite, the first constituted of palisade crystals grown perpendicular to the laminations over extremely contracted Mg-silicate remnants and replacing them, and the second with uneven thickness and chaotic orientation, both precipitated directly in matrix shrinkage pores (Figure 15). Carramal et al. [24] interpreted that the palisade crystals formed within the early filling of matrix shrinkage pores and that the orientation parallel to the matrix indicates a subaqueous origin (i.e., syneresis), most likely related to changes in water chemistry (salinity or $\alpha\text{H}_2\text{O}$). The authors also suggested that further matrix dissolution could be an internal source of Mg for carbonate precipitation. These diagenetic carbonates are strikingly similar to “beef” calcite, a term used for sub-vertical, fibrous calcite veins filling sub-horizontal fractures in and around organic-rich shales ([122,123] and references therein). Though extensive research regarding fracture formation and calcite source exists, there is no consensus yet on the origin of these veins [123].

In theory, horizontal fractures cannot form under lithostatic burial conditions, as the main stress is vertical and compressive, caused by gravity, while horizontal stress is minimal [124]. However, horizontal fractures may form where (1) tectonism results in horizontal compressive stress or (2) the tensile strength of a rock is the smallest perpendicular to bedding [125–127]. Non-tectonic fractures are formed in shales mostly due to their ultra-low permeability, which promotes overpressure build up [128], and diagenetic alterations, changing the mechanical properties of rocks, porosity, and amount of formation water [129,130]. There are several mechanisms capable of generating non-tectonic fractures in shales, which range from syneresis, sediment loading or compaction, seismic activity, authigenic mineralization, clay transformation, silica diagenesis, pressure solution, and hydrocarbon-generating processes [128,131]. Though several of these processes generate predominately sub-vertical or chaotic fractures (sediment loading, seismic activity, and opal-A to opal-CT transformation), processes capable of creating sub-horizontal fractures are found in all stages of diagenesis. The relation between lamellar carbonates and blocky dolomite indicates that these were precipitated at a similar time (see Figure 5E of Carramal et al. [24]). Furthermore, the strongly parallel orientation of the lamellar carbonates with the matrix lamination would restrain lamellar carbonate formation to shallow, pre-burial conditions. Processes that could result in the observed sub-horizontal shrinkage during eodiagenesis include syneresis [131] and clay transformation [24].

Salinity variations may promote the generation of shrinkage cracks near the sediment–water interface in sediments rich in smectites by the dehydration of the swelling clays [131]. McMahon et al. [131] showed that such conditions can produce sub-horizontal cracks in shallow sediments, and Carramal et al. [24] suggested that this, associated with matrix dissolution, is the most likely mechanism for generating the sub-horizontal pore network in the Pre-salt. The transformation of stevensite into kerolite in the Pre-salt, where a more hydrated phase (smectite) transforms into a less hydrated phase (kerolite), may have led to structural water expulsion and clay shrinkage [24]. Some studies on the evolution of clays in the Pre-salt by Silva et al. [50] and Netto et al. [52] suggested that kerolite formed directly from pore waters or from a precursor gel and were later transformed into stevensite due to increasing pH and decreasing Mg/Si through kerolite–stevensite-interstratified aggregates. However, Ramnani et al. [40] indicated that the increase of kerolite crystallinity and the predominance of kerolite in kerolite–stevensite mixed layers is related to increasing burial and temperature. A similar general trend of increasing dehydration with burial is also observed in the transformation of smectites to illites or to chlorites [132–135]. The transformation of stevensite to kerolite in the Pre-salt succession would occur through Equation (7):



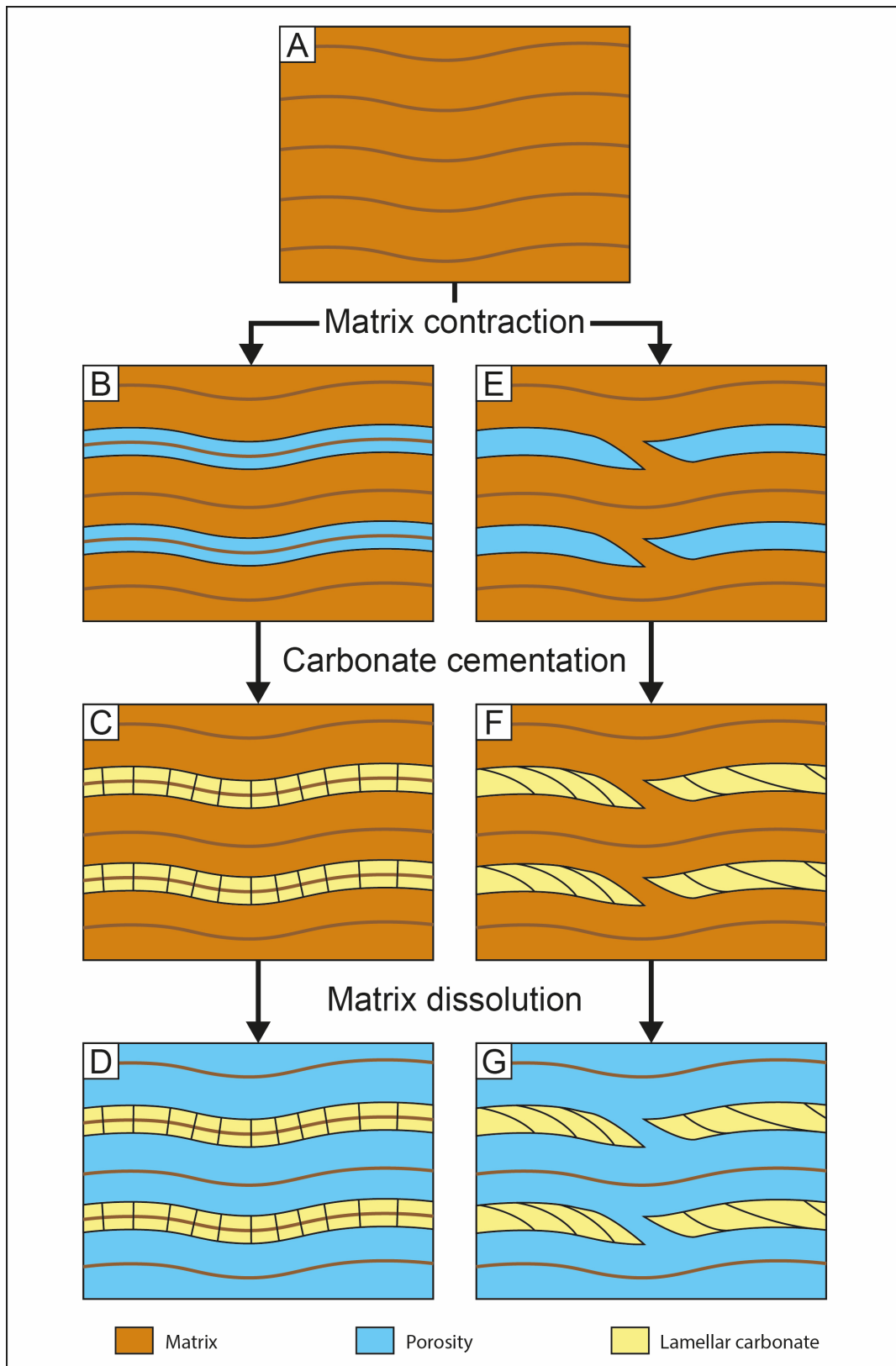


Figure 15. Schematic representation of two possible pathways for lamellar carbonate formation (modified from Carramal et al. [24]). The initial stage of laminated mud deposition (A) may follow two paths for lamellar carbonate precipitation. The left pathway shows extremely contracted matrix remnants (B) serving as a nucleus for perpendicular carbonate formation (C), which may be followed by complete matrix dissolution (D). The right pathway shows matrix contraction (E) followed by lamellar dolomite filling the shrinkage pores (F). Complete matrix dissolution creates floating lamellar carbonates (G), as also seen in the left pathway (D).

Carramal et al. [24] also reported the carbonate cementation and replacement of the clay envelopes of stevensite–kerolite ooids. These features formed in a similar fashion to the described processes of matrix shrinkage and replacement but with carbonate orientation perpendicular to particle surfaces. Although we were unable to find any preserved ooids, abundant reworked ooids occurred, with envelopes completely replaced or cemented by calcite or dolomite, which became extremely abraded during redeposition.

Layers or levels rich in peloids display more intense replacement by dolomite, silica, and calcite aggregates. This may be related to the higher original porosity and permeability of these levels than the laminated matrix, which would facilitate fluid percolation. Or this may be a different composition of the peloids. Preferential calcite precipitation in peloidal levels would explain the common occurrence of engulfed peloids in spherulites and shrubs (Figure 10). Likewise, microcrystalline and blocky dolomite most often preferentially replaced layers rich in peloids and detritals.

The replacement of Mg-clays by microcrystalline calcite in mudstones is similar to some features found in laminar calcretes with abiogenic features (alpha calcretes of 90), with irregular and “ribbon” shapes (Figures 6B and 12I). The change from spherulitic and fascicular calcite precipitation to microcrystalline calcite may indicate a decrease in alkalinity and/or silica activity [14,136–138]. The presence of spherulite remnants in thicker layers suggests that microcrystalline calcite may be, at least partially, the result of spherulite recrystallization, though direct matrix replacement seems to be the predominant process. Their lenticular shapes are also indicative of replacive–displacive precipitation.

6.4. Mesodiagenetic/Hydrothermal Interactions

We found only three carbonate phases that may be considered “late-stage” or that at the very least indicate higher precipitation temperatures. The first corresponds to saddle dolomite, characteristically formed under high temperature conditions under burial or hydrothermal conditions [49,139–143] (Figure 16A,B). The second is dawsonite ($\text{NaAl}(\text{OH})_2\text{CO}_3$) (Figure 16C), originally identified in the Pre-salt by Farias et al. [15] and by Lima and De Ros [16]. The third corresponds to coarse macrocrystalline calcite (Figure 16D). All three occur as cements in matrix dissolution and vugular pores (Figures 8F and 16B), though saddle dolomite also appears as matrix replacement (Figures 8E and 16A).

In their studies of the Campos Basin Pre-salt deposits, Lima et al. [19] found evidence of high homogenization temperatures (152 °C) for saddle dolomite and macrocrystalline calcite, which allied to their fault-associated paragenetic assemblage (macrocrystalline quartz, Sr-barite, celestine, fluorite, dickite, sphalerite, galena, other metallic sulfides, and bitumen) and led them to interpret these precipitates to be derived from burial hydrothermal fluids. Furthermore, the authors presented isotopic data ($\delta^{13}\text{C}$, $\delta^{18}\text{O}$, and $^{87}\text{Sr}/^{86}\text{Sr}$) that showed the interaction with the host rock and/or mixture of hydrothermal fluids with basinal fluids. These homogenization temperatures and isotopic data agree with the published data from Poros et al. [144], and Girard and San Miguel [145] for the analogous Kwanza Basin hydrothermal assemblage. Lima et al. [19] suggested that the hydrothermal fluids in the Campos Basin Pre-salt deposits are most likely a result of the interaction of several fluids derived from granitic–gneissic basement, rift sedimentary succession, Early and Late Cretaceous and Paleogene magmatism, and mantle exhumation and serpentinization. However, isotopic and fluid inclusion data presented by Lima et al. [19] are mostly related to late-stage pore-filling saddle dolomite or completely silicified and dolomitized rocks. Carvalho et al. [23] published a large amount of isotopic data from bulk rock geochemical analysis in 21 wells of the Tupi Field of Santos Basin, along with petrographic analysis. They found no clear hydrothermal modification of isotopes in their samples, though the authors noted that their samples did not show pervasive alteration as those analyzed by Lima et al. [19] and that saddle dolomite was closely associated with faulting, which suggested a hydrothermal origin for these minerals.

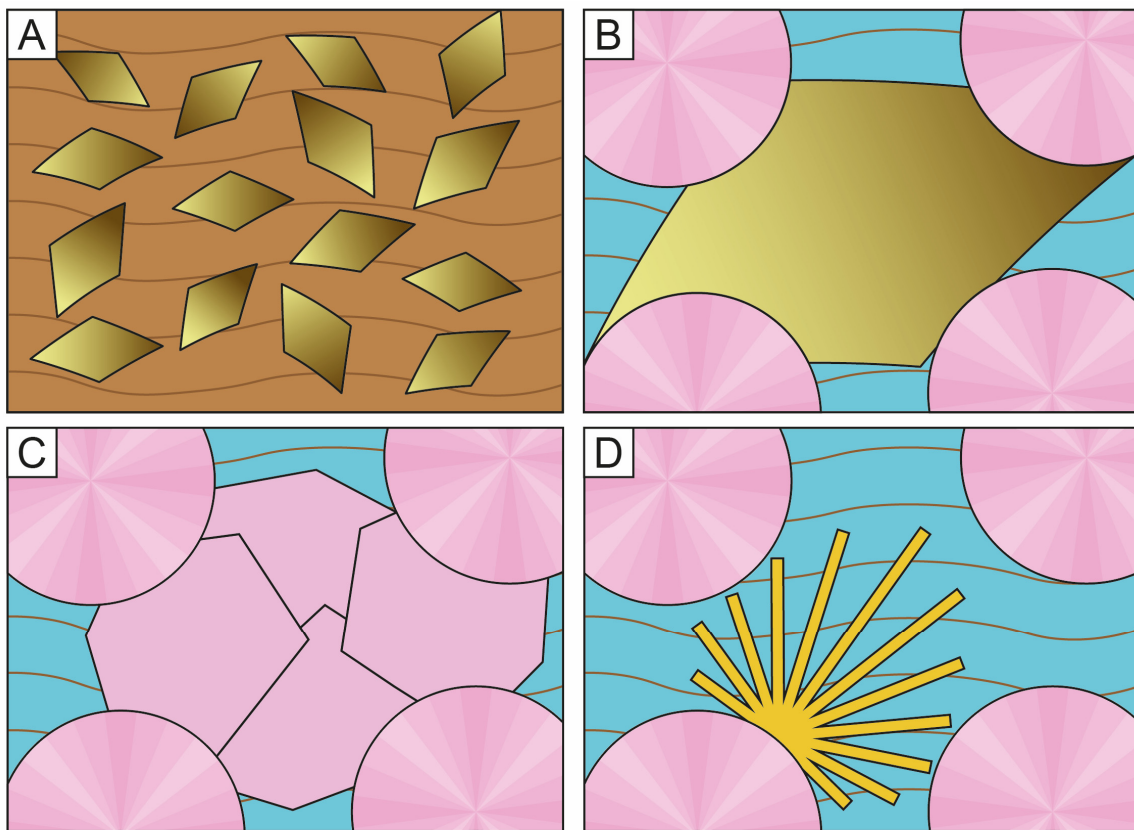


Figure 16. Schematic representation of the main mesodiagenetic relations between clays and carbonates. (A) Saddle dolomite replacing matrix. (B) Saddle dolomite partially filling matrix-dissolution pores. (C) Coarse, macrocrystalline calcite partially filling matrix-dissolution pores. (D) Dawsonite partially filling matrix-dissolution pores.

Although several authors interpret saddle dolomite as related to hydrothermal fluid flow (e.g., [10,19,112,146,147]), Machel and Lonnee [49] and Spötl and Pitman [139] have indicated that it may be related only to high temperature conditions (>80 °C) and not necessarily to hydrothermalism. Furthermore, magma-derived hydrothermal fluids are usually acidic and commonly result in the development of large-scale carbonate dissolution [146,148]. This feature is observed in some of the studied samples, where saddle dolomite is partially dissolved, but seems incongruent with samples where the matrix is partially replaced by saddle dolomite. As previously discussed, Mg-clays are extremely prone to dissolution and would not resist acidic hydrothermal fluid percolation. An alternative origin for saddle dolomite is from basinal brines under burial ([146] and references therein [113,149–152]). These fluids are highly saline and concentrated waters with varied origins, such as modified seawater (e.g., [102,143,153]), post-evaporite brines ([146] and references therein), deeply buried mudstones [143], or alteration of mafic/ultramafic rocks [143].

Lima and De Ros [16] showed the burial evolution of the Campos Basin deposits reaching close to 4.5 km and circa 111 °C, high enough temperatures for saddle dolomite formation. The Barra Velha Formation of the Santos Basin suffered higher burial depths than the described Campos Basin deposits, reaching up to 7 km depths, though averaging around 5 km. This implies that the maximum temperature for the BVF is likely higher than its Campos Basin equivalents. As such, saddle dolomite could form without the necessity of an external fluid in the BVF, as long as Ca/Mg ratios and HCO_3^- were sufficient. Stevensite transformation into kerolite as well as their large-scale dissolution could source Ca^{2+} and Mg^{2+} ions [154], creating highly concentrated brines capable of precipitating dolomite. Furthermore, early dolomite crystals may serve as a source for further

precipitation during hydrothermal dolomitization by partially consuming earlier phases of dolomite and reprecipitating as overgrowths or as recrystallization phases [114–121]. Although most saddle dolomite precipitation described in the literature are vugular or fracture-filling cements, some cases also occur where previously formed early dolomite are replaced/recrystallized by hydrothermal saddle dolomite (e.g., [153,155]). Therefore, at least part of the matrix-replacive saddle dolomite may be the result of eodiagenetic blocky dolomite recrystallization when subjected to Mg-rich fluids derived from the dissolution or transformations of Mg-clays.

Lima et al. [19] also interpreted coarse, late-stage calcite cement as hydrothermal according to its isotopic composition and fluid inclusion data, precipitated from a similar fluid as saddle dolomite. In fact, coarse calcite associated with saddle dolomite from hydrothermal fluids has been observed in several locations, usually occurring after significant dolomite precipitation (e.g., [113,118,121,143,153]). Its precipitation is usually related to a decrease in Mg^{2+} from dolomite formation and an increase in Ca^{2+} by calcite dissolution [113,156]. Considering the paucity of macrocrystalline calcite in the studied samples of the BVF and its association with saddle dolomite and dawsonite, an origin related to depleting hydrothermal fluids is likely.

Dawsonite is related to alkaline fluids with high Al^{3+} , Na^+ , and HCO_3^- and high CO_2 pressures [157]. The most common origin for this mineral is the alteration in albite in sandstones under high pCO_2 (e.g., [158] and references therein), though they have also been related to the hydrothermal activity associated with intrusive or volcanic rocks [159,160] and under shallow conditions through the reaction of Na^+ - HCO_3^- rich brines and bacterial CO_2 (e.g., [161]). Lima and De Ros [16] attributed the dawsonite presence in the Pre-salt to hydrothermal activity due to its association with saddle dolomite and Sr-barite cements. The source of CO_2 for dawsonite precipitation has been shown to be magmatic in several other studies (e.g., [157,158,160]). Our data seem to agree with a late-stage, hydrothermal origin for dawsonite, associated with saddle dolomite cementation.

7. Conclusions

The analysis of different carbonate and clay-mineral phases in five wells from three fields of the Aptian Pre-salt succession from Santos Basin allowed us to acquire several observations and inferences regarding the mechanisms and conditions involved in their formation. These processes were divided according to their relative timing of occurrence as syngenetic, eodiagenetic, and mesodiagenetic/hydrothermal.

- The main syngenetic interactions included the deposition of the magnesian clay laminated matrices, peloids, and ooids and the precipitation of fascicular calcite aggregates upon the sediment–water interface.
- The main eodiagenetic interactions include the widespread formation of spherulites and shrubs replacing and displacing the matrix, the precipitation of blocky calcite and dolomite replacing the matrix or as rims covering calcite aggregates, the precipitation of lamellar carbonates in pores formed by shrinkage of the matrix, the replacement and cementation of clay ooids, and the precipitation of microcrystalline calcite, dolomite, and silica replacing the matrix.
- The main mesodiagenetic/hydrothermal interactions are mostly related to cementation by saddle dolomite, macrocrystalline calcite, and dawsonite after significant matrix dissolution.
- The fast precipitation of syngenetic calcite shrubs occurred under high ionic supply conditions. The common occurrence of peloids within preferential growth layers in shrubs indicates that clay and carbonate precipitation was concomitant and mostly controlled by the rate of precipitation of each mineral.
- The interruption and deformation of the clay matrix laminations by the calcite spherulites and shrubs indicate that the matrix was deposited as Mg-clay particles and was replaced and displaced by the calcite aggregates still in an unconsolidated state.

- The lamellar carbonates were formed initially by filling the matrix shrinkage pores and later covered by palisade crystals perpendicular to matrix orientation. A similar pattern is observed in the replacement and cementation of the clay envelopes of the ooids.
- An original HMC composition of some aggregates could explain the wide variation in the recrystallization patterns observed in the calcite spherulites and shrubs, as well as their local pseudomorphous dolomitization.
- The common replacement of the matrix by blocky dolomite crystals was favored due to the instability of stevensite during eodiagenesis.
- The occurrence of rounded, inclusion-rich cores in blocky calcite and dolomite may indicate a recrystallization of an initial highly defective phase such as proto-dolomite or VHMC, followed by a further precipitation of more stoichiometric carbonates.
- The preferential replacement of peloidal levels by calcite and dolomite likely occurred due to their higher permeability and specific surface.
- The replacement of the matrix by microcrystalline, instead of spherulitic calcite, likely occurred due to decreased alkalinity and/or silica concentration.
- Saddle dolomite and dawsonite precipitated mostly through matrix dissolution and replacement possibly by hydrothermal fluids or alternatively as a result of the cementation and recrystallization of early blocky dolomite by evolved brines, not related to hydrothermal circulation, during burial. A mesodiagenetic origin without hydrothermal influence is suggested by the widespread distribution of saddle dolomite in wells away from major faults that could correspond to conduits for the focused flow of such fluids [19]. Macrocrystalline calcite cemented dissolution pores after significant dolomite precipitation.

These observations on the timing and controls of carbonate–clay interactions in the in situ Pre-salt rocks are essential to understand how these deposits were formed and evolved to constitute the giant petroleum reservoirs presently under exploration and production.

Supplementary Materials: The following supporting information can be downloaded at: <https://www.mdpi.com/article/10.3390/min14020191/s1>, Figure S1: Diffractogram displaying the characteristic peaks of smectite with the added re-heated and EG-solvated method described by Christidis and Koutsopoulou [39] indicating little re-expansion, which suggests stevensitic composition for the clay minerals; Figure S2: Diffractogram displaying the characteristic kerolite peak with no changes during expansion and heating steps; Figure S3: Diffractogram showing characteristic peaks of smectite with re-expansion in the second solvation step, which indicates saponite/hectorite composition; Figure S4: Diffractogram showing the characteristic behaviour of smectites together with the characteristic peak of kerolite. The broad shoulder associated to kerolite in this sample indicates a kerolite-smectite interstratification; Figure S5: Diffractogram displaying the characteristic mica/illite peak together with smectite peaks, most likely constituting illite-smectite interstratifications.

Author Contributions: Conceptualization, A.B.S.S. and L.F.D.R.; investigation, A.B.S.S., T.D.S., E.C., S.D.A., W.F. and T.H.; writing—original draft preparation, A.B.S.S.; writing—review and editing, L.F.D.R. and A.G.R.; visualization, A.B.S.S., W.F. and T.H.; supervision, L.F.D.R.; project administration, A.M. and R.B.; funding acquisition, F.D.V. All authors have read and agreed to the published version of the manuscript.

Funding: This research is part of a larger project funded by Equinor Brazil through the R&D levy regulation, project number 21761-2.

Data Availability Statement: The data presented in this study are available on request to the corresponding author. Some data are not publicly available, as it is propriety of Equinor.

Acknowledgments: This paper is part of the PhD research of the first author. We acknowledge the support and funding from Equinor Brazil and the support of ANP (Brazil's National Oil, Natural Gas and Biofuels Agency) through the R&D levy regulation. We also acknowledge the Institute of Petroleum and Natural Resources (IPR) of the Pontifical Catholic University of Rio Grande do Sul (PUCRS) for the infrastructure and support. Furthermore, we also would like to thank the support of the Postgraduate Program in Geosciences (PPGGeo) of the Federal University of Rio Grande do

Sul (UFRGS), and the Brazilian Agência Nacional de Petróleo, Gás Natural e Biocombustíveis (ANP) for permitting access to well cores and releasing samples and thin sections for analysis through the R&D levy regulation. Argos Schrank would further like to thank the Brazilian Conselho Nacional de Pesquisa (CNPq) for funding the first year of the PhD project.

Conflicts of Interest: The authors declare no conflicts of interest.

References

1. Formigli, J. Pre-Salt Reservoirs Offshore Brazil: Perspectives and Challenges. In Proceedings of the Bank of America Energy Conference, Miami, FL, USA, 15 November 2007.
2. Carminatti, M.; Wolff, B.; Gamboa, L. New exploratory frontiers in Brazil. In Proceedings of the 19th World Petroleum Congress, Madrid, Spain, 29 June–3 July 2008.
3. Gabrielli, J.S. A indústria de petróleo e gás natural. In Proceedings of the III Fórum do Instituto Brasileiro de Executivos de Finanças de Óleo e Gás, Rio de Janeiro, Brazil, 18 March 2022; p. 24.
4. Gomes, P.O.; Kilsdonk, B.; Minken, J.; Grow, T.; Barragan, R. The Outer High of the Santos Basin, Southern São Paulo Plateau, Brazil: Pre-Salt Exploration Outbreak, Paleogeographic Setting, and Evolution of the Syn-Rift Structures. In Proceedings of the AAPG International Conference and Exhibition, Cape Town, South Africa, 26–29 October 2008.
5. Sabato Ceraldi, T.; Green, D. Evolution of the South Atlantic lacustrine deposits in response to Early Cretaceous rifting, subsidence and lake hydrology. In *Petroleum Geoscience of the West Africa Margin*; Geological Society of London Special Publication 438; Sabato Ceraldi, T., Hodgkinson, R.A., Backe, G., Eds.; Geological Society of London: London, UK, 2017; pp. 77–98.
6. Saller, A.; Rushton, S.; Buambua, L.; Inman, K.; Mcneil, R.; Dickson, J.A.D. Pre-Salt stratigraphy and depositional systems in the Kwanza Basin, offshore Angola. *AAPG Bull.* **2016**, *100*, 1135–1164. [[CrossRef](#)]
7. Terra, G.J.S.; Spadini, A.R.; França, A.B.; Sombra, C.L.; Zambonato, E.E.; Juschaks, L.C.S.; Arienti, L.M.; Erthal, M.M.; Blauth, M.; Franco, M.P.; et al. Carbonate rock classification applied to Brazilian sedimentary basins. *Bol. Geociências Petrobras* **2010**, *18*, 9–29.
8. Wright, V.P.; Barnett, A.J. An abiotic model for the development of textures in some South Atlantic early Cretaceous lacustrine carbonates. In *Microbial Carbonates in Space and Time: Implications for Global Exploration and Production*; Special Publication 418; Bosence, D.W.J., Gibbons, K.A., Le Heron, D.P., Morgan, W.A., Pritchard, T., Vining, B.A., Eds.; Geological Society of London: London, UK, 2015; pp. 209–219.
9. Wright, V.P.; Tosca, N.A. Geochemical Model for the Formation of the Pre-Salt Reservoirs, Santos Basin, Brazil: Implications for Understanding Reservoir Distribution. In Proceedings of the AAPG Annual Convention and Exhibition, Calgary, AB, Canada, 19–22 June 2016.
10. Herlinger, R., Jr.; Zambonato, E.E.; De Ros, L.F. Influence of Diagenesis on the Quality of Lower Cretaceous Pre-salt Lacustrine Carbonate Reservoirs from Northern Campos Basin, Offshore Brazil. *J. Sediment. Res.* **2017**, *87*, 1285–1313. [[CrossRef](#)]
11. Kirkham, A.; Tucker, M.E. Thrombolites, spherulites and microbial crusts (Holkerian, Purbeckian, Aptian): Context, fabrics and origin. *Sediment. Geol.* **2018**, *374*, 69–84. [[CrossRef](#)]
12. Mercedes-Martín, R.; Brasier, A.T.; Rogerson, M.; Reijmer, J.J.G.; Vonhof, H.; Pedley, M. A depositional model for spherulitic carbonates associated with alkaline, volcanic lakes. *Mar. Pet. Geol.* **2017**, *86*, 68–191. [[CrossRef](#)]
13. Pietzsch, R.; Oliveira, D.M.; Tedeschi, L.R.; Neto, J.V.Q.; Figueiredo, M.F.; Vazquez, J.C.; de Souza, R.S. Palaeohydrology of the Lower Cretaceous pre-salt lacustrine system, from rift to post-rift phase, Santos Basin, Brazil. *Palaeogeogr. Palaeoclimatol. Palaeoecol.* **2018**, *507*, 60–80. [[CrossRef](#)]
14. Tutolo, B.M.; Tosca, N.J. Experimental examination of the Mg-silicate-carbonate system at ambient temperature: Implications for alkaline chemical sedimentation and lacustrine carbonate formation. *Geochim. Cosmochim. Acta* **2018**, *225*, 80–101. [[CrossRef](#)]
15. Farias, F.; Szatamari, P.; Bahniuk, A.; França, A.B. Evaporitic carbonates in the pre-salt of Santos Basin—Genesis and tectonic implications. *Mar. Pet. Geol.* **2019**, *105*, 251–272. [[CrossRef](#)]
16. Lima, B.E.M.; De Ros, L.F. Deposition, diagenetic and hydrothermal processes in the Aptian Pre-Salt lacustrine carbonate reservoirs of the northern Campos Basin, offshore Brazil. *Sediment. Geol.* **2019**, *383*, 55–81. [[CrossRef](#)]
17. Gomes, J.P.; Bunevich, R.B.; Tedeschi, L.R.; Tucker, M.E.; Whitaker, F.F. Facies classification and patterns of lacustrine carbonate deposition of the Barra Velha Formation, Santos Basin, Brazilian Pre-salt. *Mar. Pet. Geol.* **2020**, *113*, 104–176. [[CrossRef](#)]
18. Hosa, A.; Wood, R.A.; Corbett, P.W.M.; de Souza, R.S.; Roemers, E. Modelling the impact of depositional and diagenetic processes on reservoir properties of the crystal-shrub limestones in the ‘Pre-Salt’ Barra Velha Formation, Santos Basin, Brazil. *Mar. Pet. Geol.* **2020**, *112*, 104100. [[CrossRef](#)]
19. Lima, B.E.M.; Tedeschi, L.R.; Pestilho, A.L.S.; Santos, R.V.; Vazquez, J.C.; Guzzo, J.V.P.; De Ros, L.F. Deep-burial hydrothermal alteration of the Pre-Salt carbonate reservoirs from northern Campos Basin, offshore Brazil: Evidence from petrography, fluid inclusions, Sr, C and O isotopes. *Mar. Pet. Geol.* **2020**, *113*, 104143. [[CrossRef](#)]
20. Pietzsch, R.; Tedeschi, L.R.; Oliveira, D.M.; dos Anjos, C.W.D.; Vazquez, J.C.; Figueiredo, M.F. Environmental conditions of deposition of the Lower Cretaceous lacustrine carbonates of the Barra Velha Formation, Santos Basin (Brazil), based on stable carbon and oxygen isotopes: A continental record of pCO₂ during the onset of the Oceanic Anoxic Event 1a (OAE 1a) interval? *Chem. Geol.* **2020**, *535*, 119457.

21. Wright, V.P.; Barnett, A.J. The textural evolution and ghost matrices of the Cretaceous Barra Velha Formation carbonates from the Santos Basin, offshore Brazil. *Facies* **2020**, *66*, 18. [[CrossRef](#)]
22. Carvalho, M.D.; Fernandes, F.L. Pre-Salt Depositional System: Sedimentology, Diagenesis, and Reservoir Quality of the Barra Velha Formation, as a Result of the Santos Basin Tectono-Stratigraphic Development. In *The Supergiant Lower Cretaceous Pre-Salt Petroleum Systems of the Santos Basin, Brazil, AAPG Memoir 124*; Mello, M.R., Yilmaz, P.O., Katz, B.J., Eds.; AAPG and Brazilpetro studies: Tulsa, OK, USA, 2021; pp. 121–154.
23. Carvalho, A.M.A.; Hamon, Y.; Souza, O.G., Jr.; Carramal, N.G.; Collard, N. Facies and diagenesis distribution in an Aptian pre-salt carbonate reservoir of the Santos Basin, offshore Brazil: A comprehensive quantitative approach. *Mar. Pet. Geol.* **2022**, *141*, 105708. [[CrossRef](#)]
24. Carramal, N.G.; Oliveira, D.M.; Cacula, A.S.M.; Cuglieri, M.A.A.; Rocha, N.P.; Viana, S.M.; Toledo, S.L.V.; Pedrinha, S.; De Ros, L.F. Paleoenvironmental insights from the deposition and diagenesis of Aptian Pre-Salt magnesium silicates from the Lula Field, Santos Basin, Brazil. *J. Sediment. Res.* **2022**, *92*, 12–31. [[CrossRef](#)]
25. Wright, V.P. The mantle, CO₂ and the giant Aptian chemogenic lacustrine carbonate factory of the South Atlantic: Some carbonates are made, not born. *Sedimentology* **2022**, *69*, 47–73. [[CrossRef](#)]
26. Herlinger, R.; De Ros, L.F.; Surmas, R.; Vidal, A. Residual oil saturation investigation in Barra Velha Formation reservoirs from the Santos Basin, Offshore Brazil: A sedimentological approach. *Sediment. Geol.* **2023**, *448*, 106273. [[CrossRef](#)]
27. Moreira, J.L.P.; Madeira, C.V.; Gil, J.A.; Machado, M.A.P. Bacia de Santos. *Bol. Geociências Petrobras* **2007**, *15*, 531–554.
28. Freitas, V.A.; Travassos, R.M.; Cardoso, M.B. Bacia de Santos: Sumário Geológico e Setores em Oferta. In Proceedings of the Décima Sexta Rodada de Licitações, ANP, Rio de Janeiro, Brazil, 30 July 2019.
29. Milani, E.J.; Rangel, H.D.; Bueno, G.V.; Stica, J.; Winter, W.; Caixeta, J.M.; Neto, O.C.P. Bacias Sedimentares Brasileiras: Cartas Estratigráficas. *Bol. Geociências Petrobras* **2007**, *15*, 183–205.
30. Gamboa, L.A.P.; Machado, M.A.P.; Silva, D.P.; Freitas, J.T.R.; Silva, S.R.P. Evaporitos estratificados no Atlântico Sul: Interpretação sísmica e controle tectono-estratigráfico na Bacia de Santos. In *Sal: Geologia e Tectônica*; Mohriak, W., Szatmari, P., Anjos, S.M.C.d., Eds.; Beca Edições: São Paulo, Brazil, 2008; pp. 178–187.
31. Dias, J.L. Tectônica, estratigrafia e sedimentação no Andar Aptiano da margem leste brasileira. *Bol. Geociências Petrobras* **2005**, *13*, 7–25.
32. Mohriak, W.U. Bacias Sedimentares da Margem Continental Brasileira. In *Geologia, Tectônica e Recursos Minerais do Brasil*; Bizzi, L.A., Schobbenhaus, C., Vidotti, R.M., Gonçalves, J.H., Eds.; CPRM: Brasília, Brazil, 2003; pp. 87–165.
33. Riccomini, C.; Sant’Anna, L.G.; Tassinari, C.C.G. Pré-sal: Geologia e exploração. *Rev. USP* **2012**, *95*, 33–42. [[CrossRef](#)]
34. De Ros, L.F.; Oliveira, D.M. An operational classification system for the South Atlantic pre-salt rocks. *J. Sediment. Res.* **2023**, *93*, 693–704. [[CrossRef](#)]
35. Terry, R.D.; Chilingar, C.V. Summary of “Concerning some additional aids in studying sedimentary formations” by M. S. Shvetsov. *J. Sediment. Petrol.* **1955**, *25*, 229–234. [[CrossRef](#)]
36. Flügel, E. *Microfacies Analysis of Limestones*; Springer: New York, NY, USA, 1982; p. 633.
37. De Ros, L.F.; Golberg, K.; Abel, M.; Victoreti, F.; Mastella, M.; Castro, E. Advanced acquisition and management of petrographic information from reservoir rocks using the Petroledge(r) System. In Proceedings of the AAPG Annual Convention and Exhibition, Long Beach, CA, USA, 1–4 April 2007.
38. Dickson, J.A. Modified Staining Technique for Carbonates in Thin Sections. *Nature* **1965**, *205*, 587. [[CrossRef](#)]
39. Christidis, G.E.; Koutsopoulou, E. A simple approach to the identification of trioctahedral smectite by X-ray diffraction. *Clay Miner.* **2013**, *48*, 687–696. [[CrossRef](#)]
40. Ramnani, C.W.; Santos, J.F.; Parizek-Silva, Y.; Madrucci, V.; Santos, M.R.F.M.; Araújo, C.C. Diagenesis of Magnesian Clay Minerals in Santos Basin (Aptian). In Proceedings of the AIPEA—XVII International Clay Conference, Istanbul, Turkey, 25–29 July 2022.
41. Kendall, A.C. Fascicular-optic calcite: A replacement of bundled acicular carbonate cements. *J. Sediment. Petrol.* **1977**, *47*, 1056–1062. [[CrossRef](#)]
42. Pozo, M.; Calvo, J.P. Na Overview of Authigenic Magnesian Clays. *Minerals* **2018**, *8*, 520. [[CrossRef](#)]
43. Chafetz, H.S.; Guidry, S.A. Bacterial shrubs, crystal shrubs, and ray-crystal shrubs: Bacterial vs. abiotic precipitation. *Sediment. Geol.* **1999**, *126*, 57–74. [[CrossRef](#)]
44. Riding, R.; Virgone, A. Hybrid Carbonates: In situ abiotic, microbial and skeletal co-precipitates. *Earth-Sci. Rev.* **2020**, *208*, 103300. [[CrossRef](#)]
45. Chilingar, G.V.; Bissel, H.J.; Wolf, K.H. Diagenesis of Carbonate Rocks. In *Diagenesis in Sediments, Developments in Sedimentology*; Larsen, G., Chilingar, G.V., Eds.; Elsevier: Amsterdam, The Netherlands, 1967; Volume 8, pp. 179–322.
46. Choquette, P.W.; Pray, L.C. Geologic Nomenclature and Classification of Porosity in Sedimentary Carbonates. *AAPG Bull.* **1970**, *54*, 207–250.
47. Worden, R.H.; Burley, S.D. Sandstone diagenesis: The evolution of sand to stone. In *Sandstone Diagenesis: Recent and Ancient*; Burley, S.D., Worden, R.H., Eds.; International Association of Sedimentologists Blackwell Publishing Ltd.: Malden, MA, USA, 2003; pp. 1–44.
48. Morad, S.; Ketzer, J.M.; De Ros, L.F. Spatial and temporal distribution of diagenetic alterations in siliciclastic rocks: Implications for mass transfer in sedimentary basins. *Sedimentology* **2000**, *47*, 95–120. [[CrossRef](#)]

49. Machel, H.G.; Lonnee, J. Hydrothermal dolomite—A product of poor definition and imagination. *Sediment. Geol.* **2002**, *152*, 163–171. [[CrossRef](#)]
50. Silva, M.D.; Gomes, M.E.B.; Mexias, A.S.; Pozo, M.; Drago, S.M.; Célia, R.S.; Silva, L.A.C.; Netto, P.; Gomes, L.B.; Porcher, C.C.; et al. Mineralogical Study of Levels with Magnesian Clay Minerals in the Santos Basin, Aptian Pre-Salt Brazil. *Minerals* **2022**, *11*, 970. [[CrossRef](#)]
51. Netto, P.R.A.; Pozo, M.; Silva, M.D.; Mexias, A.S.; Gomes, M.E.B.; Borghi, L.; Rios-Netto, A.M. b Authigenic Mg-Clay assemblages in the Barra Velha Formation (Upper Cretaceous) from Santos Basin (Brazil): The Role of Syngenetic and Diagenetic Processes. *Appl. Clay Sci.* **2021**, *216*, 106339. [[CrossRef](#)]
52. Netto, P.R.A.; Pozo, M.; Silva, M.D.; Gomes, M.E.B.; Mexias, A.; Ramnani, C.W.; Parizek-Silva, Y.; Borghi, L.; Rios-Netto, A.d.M. Paleoenvironmental implications of authigenic magnesian clay formation sequences in the Barra Velha Formation (Santos Basin, Brazil). *Minerals* **2022**, *12*, 200. [[CrossRef](#)]
53. Grotzinger, J.P.; Knoll, A.H. Anomalous carbonate precipitates: Is the Precambrian the key to the Permian? *Palaio* **1995**, *10*, 578–596. [[CrossRef](#)] [[PubMed](#)]
54. Grotzinger, J.P.; Knoll, A.H. Stromatolites in Precambrian carbonates: Evolutionary mileposts or environmental dipsticks? *Annu. Rev. Earth Planet. Sci.* **1999**, *27*, 313–358. [[CrossRef](#)]
55. Sami, T.T.; James, N.P. Peritidal carbonate platform growth and cyclicity in an early Proterozoic foreland basin, upper Pethei Group, northwest Canada. *J. Sediment. Res.* **1994**, *64*, 111–131.
56. Pope, M.C.; Grotzinger, J.P.; Schreiber, B.C. Evaporitic subtidal stromatolites produced by in situ precipitation: Textures, facies associations, and temporal significance. *J. Sediment. Res.* **2000**, *70*, 1139–1151. [[CrossRef](#)]
57. Riding, R. Abiogenic, microbial and hybrid authigenic carbonate crusts: Components of Precambrian stromatolites. *Geol. Croat.* **2008**, *61*, 73–103. [[CrossRef](#)]
58. Coniglio, M.; Frizzell, R.; Pratt, B.R. Reef-capping laminites in the Upper Silurian carbonateto-evaporite transition, Michigan Basin, south-western Ontario. *Sedimentology* **2004**, *51*, 653–668. [[CrossRef](#)]
59. Pruss, S.B.; Bottjer, D.J.; Corsetti, F.A.; Baud, A. A global marine sedimentary response to the end-Permian mass extinction: Examples from southern Turkey and the western United States. *Earth-Sci. Rev.* **2006**, *78*, 193–206. [[CrossRef](#)]
60. Pentecost, A. The formation of travertine shrubs: Mammoth hot springs, Wyoming. *Geol. Mag.* **1990**, *294*, 159–168. [[CrossRef](#)]
61. De Ros, L.F. Syngenetic, Diagenetic and Hydrothermal Processes in the Pre-Salt Sag Section of Santos and Campos Basins. In Proceedings of the Second EAGE Conference on Pre-Salt Reservoirs, Online, 8–10 September 2021.
62. Tosca, N.J.; Wright, V.P. Diagenetic pathways linked to labile Mg-clays in lacustrine carbonate reservoirs: A model for the origin of secondary porosity in the Cretaceous pre-salt Barra Velha Formation, offshore Brazil. In *Reservoir Quality of Clastic and Carbonate Rocks: Analysis, Modelling and Prediction*; Armitage, P.J., Butcher, A.R., Churchill, J.M., Csoma, A.E., Hollis, C., Lander, R.H., Omma, J.E., Worden, R.H., Eds.; Geological Society, Special Publications: London, UK, 2015; Volume 435, pp. 33–46.
63. French, M.W.; Worden, R.H.; Mariani, E.; Larese, R.E.; Mueller, R.R.; Kliewer, C.E. Microcrystalline quartz generation and the preservation of porosity in sandstones: Evidence from the Upper Cretaceous of the Subhercynian Basin, Germany. *J. Sediment. Res.* **2012**, *82*, 422–434. [[CrossRef](#)]
64. French, M.W.; Worden, R.H. Orientation of microcrystalline quartz in the Fontainebleau Formation, Paris Basin and why it preserves porosity. *Sediment. Geol.* **2013**, *284–285*, 149–158. [[CrossRef](#)]
65. Raigemborn, M.S.; Gómez-Peral, L.E.; Krause, J.M.; Matheos, S.D. Controls on clay minerals assemblages in an early Paleogene nonmarine succession: Implications for the volcanic and paleoclimatic record of extra-andean Patagonia, Argentina. *J. S. Am. Earth Sci.* **2014**, *52*, 1–23. [[CrossRef](#)]
66. Vazquez, M.; Bauluz, B.; Nieto, F.; Morata, D. Illitization sequence controlled by temperature in volcanic geothermal systems: The Tinguiririca geothermal field, Andean Cordillera, Central Chile. *Appl. Clay Sci.* **2016**, *134*, 221–234. [[CrossRef](#)]
67. Odin, G.S. Introduction to the Verdine Facies. In *Green Marine Clays: Oolitic Ironstone Facies, Verdine Facies, Glaucony Facies, and Celadonite-Bearing Facies, Developments in Sedimentology*; Odin, G.S., Ed.; Elsevier Science: Amsterdam, The Netherlands, 1988; Volume 45, pp. 53–56.
68. Baldermann, A.; Dietzel, M.; Mavromatis, V.; Mittermayer, F.; Warr, L.N.; Wemmer, K. The role of Fe on the formation and diagenesis of interstratified glauconite-smectite and illite-smectite: A case study of Upper Cretaceous shallow-water carbonates. *Chem. Geol.* **2017**, *453*, 21–34. [[CrossRef](#)]
69. Odin, G.S. Significance of Green Particles (Glaucony, Berthierine, Chlorite) in Arenites. In *Provenance of Arenites*; Zuffa, G.G., Ed.; NATO ASI Series; Springer: Dordrecht, Germany, 1985; Volume 148, pp. 279–307.
70. Amorosi, A. Detecting compositional, spatial, and temporal attributes of glaucony: A tool for provenance research. *Sediment. Geol.* **1997**, *109*, 135–153. [[CrossRef](#)]
71. Armelenti, G.; Goldberg, K.; Kuchle, J.; De Ros, L.F. Deposition, diagenesis and reservoir potential of non-carbonate sedimentary rocks from the rift section of Campos Basin, Brazil. *Pet. Geosci.* **2016**, *22*, 223–239. [[CrossRef](#)]
72. Kranck, K. Flocculation of Suspended Sediment in the Sea. *Nature* **1973**, *246*, 348–350. [[CrossRef](#)]
73. Kranck, K. Experiments on the significance of flocculation in the settling of fine-grained sediment in still water. *Can. J. Earth Sci.* **1980**, *17*, 1517–1526. [[CrossRef](#)]
74. Syvitski, J.P.; Asprey, K.W.; Clattenburg, D.A.; Hodg, G.D. The prodelta environment of a fjord: Suspended particle dynamics. *Sedimentology* **1985**, *32*, 83–107. [[CrossRef](#)]

75. Hill, P.S.; Miligan, T.G.; Geyer, W.R. Controls on effective settling velocity of suspended sediment in the Eel River flood plume. *Cont. Shelf Res.* **2000**, *20*, 2095–2111. [[CrossRef](#)]
76. Fox, J.M.; Hill, P.; Milligan, T.G.; Boldrin, A. Flocculation and sedimentation on the Po River Delta. *Mar. Geol.* **2004**, *203*, 95–107. [[CrossRef](#)]
77. Winterwerp, J.C.; van Kesteren, W.G.M. *Introduction to the Physics of Cohesive Sediment in the Marine Environment*; Elsevier: Amsterdam, The Netherlands, 2004; p. 466.
78. Sahin, C.; Guner, H.A.A.; Ozturk, M.; Sheremet, A. Floc size variability under strong turbulence: Observations and artificial neural network modeling. *Appl. Ocean. Res.* **2017**, *68*, 130–141. [[CrossRef](#)]
79. Arp, G.; Reimer, A.; Reitner, J. Microbialite formation in seawater of increased alkalinity, Satonda Crater Lake, Indonesia. *J. Sediment. Res.* **2003**, *73*, 105–127. [[CrossRef](#)]
80. Bontognali, T.R.; Vasconcelos, C.; Warthmann, R.J.; Bernasconi, S.M.; Dupraz, C.; Strohmenger, C.J.; McKenzie, J.A. Dolomite formation within microbial mats in the coastal sabkha of Abu Dhabi (United Arab Emirates). *Sedimentology* **2010**, *57*, 824–844. [[CrossRef](#)]
81. Burne, R.V.; Moore, L.S.; Christy, A.G.; Troitzsch, U.; King, P.L.; Carnerup, A.M.; Hamilton, P.J. Stevensite in the modern thrombolites of Lake Clifton, Western Australia: A missing link in microbialite mineralization? *Geology* **2014**, *42*, 575–578. [[CrossRef](#)]
82. Perri, E.; Tucker, M.E.; Słowakiewicz, M.; Whitaker, F.; Bowen, L.; Perrotta, I.D. Carbonate and silicate biomineralization in a hypersaline microbial mat (Mesaieed sabkha, Qatar): Roles of bacteria, extracellular polymeric substances and viruses. *Sedimentology* **2018**, *65*, 1213–1245. [[CrossRef](#)]
83. Flemming, H.-C.; Wingender, J. The biofilm matrix. *Nat. Rev. Microbiol.* **2010**, *8*, 623–633. [[CrossRef](#)] [[PubMed](#)]
84. Bertani, R.; Carozzi, A. Lagoa Feia Formation (Lower Cretaceous) Campos Basin, offshore Brazil: Rift valley type lacustrine carbonate reservoirs I. *J. Pet. Geol.* **1985**, *8*, 37–58. [[CrossRef](#)]
85. Leite, C.O.N.; Silca, C.M.A.; De Ros, L.F. Depositional and diagenetic processes in the pre-salt rift section of a Santos Basin area, SE Brazil. *J. Sediment. Res.* **2020**, *90*, 584–608. [[CrossRef](#)]
86. Chafetz, H.; Barth, J.; Cook, M.; Guo, X.; Zhou, J. Origins of carbonate spherulites: Implications for Brazilian Aptian pre-salt reservoir. *Sediment. Geol.* **2018**, *365*, 21–33. [[CrossRef](#)]
87. Tonietto, S.N.; Gomes, J.P.B.; Bunevich, R.B.; Erthal, M.M. Spherulitstone as a transitional facies responding to lake level variation—Diagenetic or depositional? In Proceedings of the AAPG IMAGE, Houston, TX, USA, 28 August–1 September 2023.
88. Rodríguez-Berriguete, A.; Dal’Bo, P.F.; Valle, B.; Borghi, L. When distinction matters: Carbonate shrubs from the Aptian Barra Velha Formation of Brazilian’s Pre-salt. *Sediment. Geol.* **2022**, *440*, 106236. [[CrossRef](#)]
89. Wright, V.P.; Barnett, A. Cyclicality and carbonate-silica gel interactions in Cretaceous alkaline lakes. In Proceedings of the AAPG Annual Convention and Exhibition, Houston, TX, USA, 6–9 April 2014.
90. Tucker, M.E.; Wright, V.P. Calcretes: An Introduction. In *Calcretes*, 2nd ed.; Tucker, M.E., Wright, V.P., Eds.; International Association of Sedimentologists, Blackwell Science: Oxford, UK, 1991; pp. 1–22.
91. Sélles-Martinez, J. Concretion morphology, classification and genesis. *Earth-Sci. Rev.* **1996**, *41*, 177–210. [[CrossRef](#)]
92. Arementeros, I. Diagenesis of carbonates in continental settings. In *Carbonates in Continental Settings, Geochemistry, Diagenesis and Applications, Developments in Sedimentology*; Alonso-Zarza, A.M., Tanner, L., Eds.; Elsevier: Oxford, UK, 2010; Volume 62, pp. 61–151.
93. Gaines, R.R.; Vorhies, J.S. Growth mechanisms and geochemistry of carbonate concretions from the Cambrian Wheeler Formation (Utah, USA). *Sedimentology* **2016**, *63*, 662–698. [[CrossRef](#)]
94. Pozo, M. Origin and evolution of magnesium clays in lacustrine environments: Sedimentology and geochemical pathways. In Proceedings of the 1st Latin American Clay Conference, Funchal, Portugal, 17–22 September 2000; pp. 117–133.
95. Galán, E.; Pozo, M. Palygorskite and sepiolite deposits in continental environments. Description, genetic patterns and sedimentary settings. In *Developments in Palygorskite—Sepiolite Research, Developments in Clay Science 3*; Singer, A., Galán, E., Eds.; Elsevier: Amsterdam, The Netherlands, 2011; pp. 125–174.
96. Tosca, N.J.; Masterson, A. Chemical controls on incipient Mg-silicate crystallization at 25 °C: Implications for early and late diagenesis. *Clay Miner.* **2014**, *49*, 165–194. [[CrossRef](#)]
97. Guggenheim, Introduction to Mg-rich clay minerals: Structure and composition. In *Magnesian Clays: Characterization, Origins and Applications—Association Internationale pour L’Étude des Argiles*; Educational Series; Pozo, M.; Galán, E. (Eds.) Digilabs Pub.: Bari, Italy, 2013; Volume 2, pp. 1–62.
98. Molnár, Z.; Pekker, P.; Dódony, I.; Pósfai, M. Clay minerals affect calcium (magnesium) carbonate precipitation and aging. *Earth Planet. Sci. Lett.* **2021**, *567*, 116971. [[CrossRef](#)]
99. Gomes, J.P. Facies, Diagenesis and Cycles within the Pre-Salt Deposits from Barra Velha Formation, Santos Basin, Offshore Brazil. Ph.D. Thesis, University of Bristol, Bristol, UK, September 2021.
100. Sibley, D.F. The origin of common dolomite fabrics; clues from the Pliocene. *J. Sediment. Res.* **1982**, *52*, 1087.
101. Budd, D.A. Dissolution of High-Mg Calcite Fossils and the Formation of Biomolds During Mineralogical Stabilization. *Carbonates Evaporites* **1997**, *7*, 74–81. [[CrossRef](#)]

102. Kirmacı, M.Z.; Yıldız, M.; Kandemir, R.; Eroğlu-Gümrük, T. Multistage dolomitization in Late Jurassic–Early Cretaceous platform carbonates (Berdiga Formation), Başoba Yayla (Trabzon), NE Turkey: Implications of the generation of magmatic arc on dolomitization. *Mar. Pet. Geol.* **2018**, *89*, 515–529. [[CrossRef](#)]
103. Lohman, K.C.; Meyers, W.J. Microdolomite inclusions in cloudy prismatic calcites: A proposed criterion for former high-magnesium calcite. *J. Sediment. Petrol.* **1977**, *47*, 1078–1088.
104. Stanienda, K.J. Carbonate phases rich in magnesium in the Triassic limestones of the eastern part of the Germanic Basin. *Carbonates Evaporites* **2016**, *31*, 387–405. [[CrossRef](#)]
105. Cotton, L.J.; Evans, D.; Beavington-Penney, S.J. The high-magnesium calcite origin of Nummulitid foraminifera and implications for the identification of calcite diagenesis. *Palaios* **2020**, *35*, 421–431. [[CrossRef](#)]
106. Ross, D.J. Botryoidal high-magnesium calcite marine cements from the Upper Cretaceous of the Mediterranean Region. *J. Sediment. Petrol.* **1991**, *61*, 349–353.
107. Gregg, J.M.; Bish, D.L.; Kaczmarek, S.E.; Machel, H.G. Mineralogy, nucleation and growth of dolomite in the laboratory and sedimentary environment: A review. *Sedimentology* **2015**, *62*, 1749–1769. [[CrossRef](#)]
108. Warren, K. Dolomite: Occurrence, Evolution and Economically Important Associations. *Earth-Sci. Rev.* **2000**, *52*, 1–81. [[CrossRef](#)]
109. Rodriguez-Blanco, J.D.; Shaw, S.; Benning, L.G. A route for the direct crystallization of dolomite. *Am. Mineral.* **2015**, *100*, 1172–1181. [[CrossRef](#)]
110. Hashim, M.S.; Kaczmarek, S.E. Experimental stabilization of carbonate sediments to calcite: Insights into the depositional and diagenetic controls on calcite microcrystal texture. *Earth Planet. Sci. Lett.* **2020**, *538*, 116235. [[CrossRef](#)]
111. Huang, H.; Wen, H.; Wen, L.; Zhang, B.; Zhou, G.; He, Y.; Wen, L.; Zhao, Y.; Jiang, H. Multistage dolomitization of deeply buried dolomite in the Lower Cambrian Canglangpu Formation, central and northern Sichuan Basin. *Mar. Pet. Geol.* **2023**, *152*, 106261. [[CrossRef](#)]
112. Liu, D.; Xu, Y.; Papineau, D.; Yu, N.; Fan, Q.; Qiu, X.; Hongmei, W. Experimental evidence for abiotic formation of low-temperature proto-dolomite facilitated by clay minerals. *Geochim. Cosmochim. Acta* **2019**, *247*, 83–95. [[CrossRef](#)]
113. Li, T.; Zhu, D.; Yang, M.; Zhang, X.; Li, P.; Lu, C.; Zou, H. Early-stage marine dolomite altered by hydrothermal fluids in the Middle Permian Maokou Formation in the eastern Sichuan Basin, Southern China. *Mar. Pet. Geol.* **2021**, *134*, 105367. [[CrossRef](#)]
114. Jones, B. Inside-Out Dolomite. *J. Sediment. Res.* **2007**, *77*, 539–551. [[CrossRef](#)]
115. Salih, N.; Mansurbeg, H.; Kolo, K.; Pr at, A. Hydrothermal Carbonate Mineralization, Calcretization, and Microbial Diagenesis Associated with Multiple Sedimentary Phases in the Upper Cretaceous Bekhme Formation, Kurdistan Region-Iraq. *Geosciences* **2019**, *9*, 459. [[CrossRef](#)]
116. Mueller, M.; Igbokwe, O.A.; Walter, B.; Pederson, C.L.; Riechelmann, S.; Richter, D.K.; Albert, R.; Gerdes, A.; Buhl, D.; Neuser, R.D.; et al. Testing the preservation potential of early diagenetic dolomites as geochemical archives. *Sedimentology* **2019**, *67*, 849–881. [[CrossRef](#)]
117. Koeshidayatullah, A.; Corlett, H.; Stacey, J.; Swart, P.K.; Boyce, A.; Robertson, H.; Whitaker, F.; Hollis, C. Evaluating new fault-controlled hydrothermal dolomitization models: Insights from the Cambrian Dolomite, Western Canadian Sedimentary Basin. *Sedimentology* **2020**, *67*, 2945–2973. [[CrossRef](#)]
118. Huang, B.; Zhang, S.; Lu, N.; Ye, N.; Zhu, B.; Ding, X.; Li, Y. Origin of dolomites in Lower-Middle Ordovician carbonate rocks in the Yingshan Formation, Gucheng Area, Tarim Basin: Evidence from petrography and geochemical data. *Mar. Pet. Geol.* **2021**, *134*, 105322. [[CrossRef](#)]
119. Kareem, K.H.; Al-Aasm, I.S.; Mansurbeg, H. Geochemical constraints of hydrothermal alteration of dolostones: An example of Lower Cretaceous Qamchuqa Formation, Kurdistan Region, northern Iraq. *Mar. Pet. Geol.* **2021**, *134*, 105337. [[CrossRef](#)]
120. Pan, L.; Hu, A.; Liang, F.; Jiang, L.; Hao, Y.; Feng, Y.; Shen, A.; Zhao, J. Diagenetic conditions and geodynamic setting of the middle Permian hydrothermal dolomites from southwest Sichuan Basin, SW China: Insights from in situ U–Pb carbonate geochronology and isotope geochemistry. *Mar. Pet. Geol.* **2021**, *129*, 105080. [[CrossRef](#)]
121. Stacey, J.; Corlett, H.; Holland, G.; Koeshidayatullah, A.; Cao, C.; Swart, P.; Crowley, S.; Hollis, C. Regional fault-controlled shallow dolomitization of the Middle Cambrian Cathedral Formation by hydrothermal fluids fluxed through basal clastic aquifer. *Geol. Soc. Am. Bull.* **2021**, *113*, 2355–2377. [[CrossRef](#)]
122. Cobbold, P.R.; Zanella, A.; Rodrigues, N.; L seth, H. Bedding-parallel fibrous veins (beef and cone-in-cone): Worldwide occurrence and possible significance in terms of fluid overpressure, hydrocarbon generation and mineralization. *Mar. Pet. Geol.* **2013**, *43*, 1–20. [[CrossRef](#)]
123. Su, A.; Bons, P.D.; Chen, H.; Feng, Y.; Zhao, J.; Song, J. Age, material source, and formation mechanism of bedding-parallel calcite beef veins: Case from the mature Eocene lacustrine shales in the Biyang Sag, Nanxiang Basin, China. *GSA Bull.* **2022**, *134*, 1811–1833. [[CrossRef](#)]
124. Sibson, R.H. Brittle-failure controls on maximum sustainable overpressure in different tectonic regimes. *AAPG Bull.* **2003**, *87*, 901–908. [[CrossRef](#)]
125. Cosgrove, J.W. The expression of hydraulic fracturing in rocks and sediments. *Geol. Soc. Lond. Spec. Publ.* **1995**, *92*, 187–196. [[CrossRef](#)]
126. Cosgrove, J.W. Hydraulic fracturing during the formation and deformation of a basin: A factor in the dewatering of low-permeability sediments. *AAPG Bull.* **2001**, *85*, 737–748.

127. Lash, G.G.; Engelder, T. An analysis of horizontal microcracking during catagenesis: Example from the Catskill delta complex. *AAPG Bull.* **2005**, *89*, 1433–1449. [[CrossRef](#)]
128. Meng, Q.; Hao, F.; Tian, J. Origins of non-tectonic fractures in shale. *Earth-Sci. Rev.* **2021**, *222*, 103825. [[CrossRef](#)]
129. Mathia, E.J.; Bowen, L.; Thomas, K.M.; Aplin, A.C. Evolution of porosity and pore types in organic-rich, calcareous, lower toarcian posidonia shale. *Mar. Pet. Geol.* **2016**, *75*, 117–139. [[CrossRef](#)]
130. Milliken, K.L.; Olson, T. Silica Diagenesis, Porosity Evolution, and Mechanical Behavior in Siliceous Mudstones, Mowry Shale (Cretaceous), Rocky Mountains, U.S.A. *J. Sediment. Res.* **2017**, *87*, 366–387. [[CrossRef](#)]
131. McMahon, S.; Hood, A.S.; McIlroy, D. The origin and occurrence of subaqueous sedimentary cracks. In *Earth System Evolution and Early Life: A Celebration of the Work of Martin Brasier*; Brasier, A.T., McIlroy, D., McLoughlin, N., Eds.; Geological Society of London: London, UK, 2017; Volume 448, pp. 295–309.
132. Curtis, C.D.; Murchison, D.G.; Berner, R.A.; Shaw, H.; Sarnthein, M.; Durand, B.; Eglinton, G.; Mackenzie, A.S.; Surdam, R.C. Clay mineral precipitation and transformation during burial diagenesis. *Philos. Trans. R. Soc. Lond. Ser. A Math. Phys. Sci.* **1985**, *315*, 91–105.
133. Foscolos, A.E. Diagenesis 7. Catagenesis of Argillaceous Sedimentary Rocks. *Geosci. Can.* **1984**, *11*, 67–75.
134. Meunier, A. *Clays*; Springer: Heidelberg, Germany, 2005; p. 486.
135. Velde, B. *Clay Minerals: A Physico-Chemical Explanation of Their Occurrence*; Developments in Sedimentology Vol. 40; Elsevier Science: Amsterdam, The Netherlands, 2000; p. 426.
136. Garcia-Ruiz, J.M. Geochemical scenarios for the precipitation of biomimetic inorganic carbonates. In *Carbonate Sedimentation and Diagenesis in the Evolving Precambrian World*; Grotzinger, J.P., James, N.P., Eds.; Society of Sedimentary Geology: Tulsa, OK, USA, 2000; Volume 67, pp. 578–596.
137. Beck, R.; Andreassen, J.-P. Spherulitic growth of calcium carbonate. *Cryst. Growth Des.* **2010**, *10*, 2934–2947. [[CrossRef](#)]
138. Meister, P.; Johnson, O.; Corsetti, F.; Neelson, K.H. Magnesium inhibition controls spherical carbonate precipitation in ultrabasic springwater (Cedars, California) and culture experiments. In *Advances in Stromatolite Geobiology*; Reitner, J., Queric, N.-V., Arp, G., Eds.; Springer: Berlin, Germany, 2010; pp. 101–121.
139. Spötl, C.; Pitman, J.K. Saddle (Baroque) Dolomite in Carbonates and Sandstones: A Reappraisal of a Burial-Diagenetic Concept. In *Carbonate Cementation in Sandstones: Distribution Patterns and Geochemical Evolution*; Morad, S., Ed.; The International Association of Sedimentologists, Blackwell Science Ltd.: Oxford, UK, 1998; pp. 437–460.
140. Al-Aasm, I.; Lonnee, J.; Clarke, J. Multiple fluid flow events and the formation of saddle dolomite: Case studies from the Middle Devonian of the Western Canada Sedimentary Basin. *Mar. Pet. Geol.* **2002**, *19*, 209–217. [[CrossRef](#)]
141. Lavoie, D.; Jackson, S.; Girard, I. Magnesium isotopes in high-temperature saddle dolomite cements in the lower Paleozoic of Canada. *Sediment. Geol.* **2014**, *305*, 58–68. [[CrossRef](#)]
142. Sirat, M.; Al-Aasm, I.S.; Morad, S.; Aldahan, A.; Al-Jallad, O.; Ceriani, A.; Morad, D.; Mansurbeg, H.; Al-Suwaidi, A. Saddle dolomite and calcite cements as records of fluid flow during basin evolution: Paleogene carbonates, United Arab Emirates. *Mar. Pet. Geol.* **2016**, *74*, 71–91. [[CrossRef](#)]
143. Mansurbeg, H.; Alsuwaidi, M.; Salih, N.; Shahorkhi, S.; Morad, S. Integration of stable isotopes, radiometric dating and microthermometry of saddle dolomite and host dolostones (Cretaceous carbonates, Kurdistan, Iraq): New insights into hydrothermal dolomitization. *Mar. Pet. Geol.* **2021**, *127*, 104989. [[CrossRef](#)]
144. Poros, Z.; Jagmiecki, E.; Luczaj, J.; Kenter, J.; Gal, B.; Correa, T.S.; Ferreira, E.; McFadden, K.A.; Elifritz, A.; Heumann, N.; et al. Origin of silica in pre-salt carbonates, Kwanza Basin, Angola. In Proceedings of the AAPG Annual Convention and Exhibition, Houston, TX, USA, 2–5 April 2017.
145. Girard, J.-P.; San Miguel, G. Evidence of High Temperature Hydrothermal Regimes in the Pre-Salt Series, Kwanza Basin, Offshore Angola. In Proceedings of the AAPG Annual Convention and Exhibition, Houston, TX, USA, 2–5 April 2017.
146. Davies, G.R.; Smith, L.B. Structurally controlled hydrothermal dolomite reservoir facies: An overview. *AAPG Bull.* **2006**, *31*, 455–468. [[CrossRef](#)]
147. Ryan, B.H.; Kaczmarek, S.E.; Rivers, J.M. Multi-Episodic Recrystallization and Isotopic Resetting of Early-Diagenetic Dolomites in Near-Surface Settings. *J. Sediment. Res.* **2021**, *91*, 146–166. [[CrossRef](#)]
148. Moore, C.H.; Wade, W.J. Burial Diagenetic Environment. In *Carbonate Reservoirs: Porosity and Diagenesis in a Sequence Stratigraphic Framework, Developments in Sedimentology*, 2nd ed.; Moore, C.H., Wade, W.J., Eds.; Elsevier: Amsterdam, The Netherlands, 2013; Volume 67, pp. 239–284.
149. Lonnee, J.; Machel, H.G. Pervasive dolomitization with subsequent hydrothermal alteration in the Clarke Lake gas field, Middle Devonian Slave Point Formation, British Columbia, Canada. *AAPG Bull.* **2006**, *90*, 1739–1761. [[CrossRef](#)]
150. Mansurbeg, H.; Morad, D.; Othman, R.; Morad, S.; Ceriani, A.; Al-Aasm, I.; Kolo, K.; Spirov, P.; Proust, J.N.; Preat, A. Hydrothermal dolomitization of the Bekhme formation (Upper Cretaceous), Zagros Basin, Kurdistan Region of Iraq: Record of oil migration and degradation. *Sediment. Geol.* **2016**, *341*, 147–162. [[CrossRef](#)]
151. Morad, S.; Al Suwaidi, M.; Mansurbeg, H.; Morad, D.; Ceriani, A.; Paganoni, N.; Al-Aasm, I. Diagenesis of a limestone reservoir (Lower Cretaceous), Abu Dhabi, United Arab Emirates: Comparison between the anticline crest and flanks. *Sediment. Geol.* **2019**, *380*, 127–142. [[CrossRef](#)]

152. Stacey, J.; Hollis, C.; Corlett, H.; Koeshidayatullah, A. Burial dolomitization driven by modified seawater and basal aquifer-sourced brines: Insights from the Middle and Upper Devonian of the Western Canadian Sedimentary Basin. *Basin Res.* **2020**, *33*, 648–680. [[CrossRef](#)]
153. Kareem, K.H.; Al-Aasm, I.; Mansurbeg, H. Structurally-controlled hydrothermal fluid flow in an extensional tectonic regime: A case study of Cretaceous Qamchuqa Formation, Zagros Basin, Kurdistan Iraq. *Sediment. Geol.* **2019**, *386*, 52–78. [[CrossRef](#)]
154. Jones, B.J.; Mumpton, F.A. Clay mineral diagenesis in lacustrine sediments. *GSA Bull.* **1986**, *1578*, 291–300.
155. Guo, C.; Chen, D.; Qing, H.; Dong, S.; Li, G.; Wang, D.; Qian, Y.; Liu, C. Multiple dolomitization and later hydrothermal alteration on the Upper Cambrian-Lower Ordovician carbonates in the northern Tarim Basin, China. *Mar. Pet. Geol.* **2016**, *72*, 295–316. [[CrossRef](#)]
156. Merino, E.; Canals, À. Self-accelerating dolomite-for-calcite replacement: Self-organized dynamics of burial dolomitization and associated mineralization. *Am. J. Sci.* **2011**, *311*, 573–607. [[CrossRef](#)]
157. Worden, R.H. Dawsonite cement in the Triassic Lam Formation, Shabwa Basin, Yemen: A natural analogue for a potential mineral product of subsurface CO₂ storage for greenhouse gas reduction. *Mar. Pet. Geol.* **2006**, *23*, 61–77. [[CrossRef](#)]
158. Cseresznyés, D.; Czuppon, G.; Király, C.; Demény, A.; Györe, D.; Forray, V.; Kovács, I.; Szabó, C.; Falus, G. Origin of dawsonite-forming fluids in the Mihélyi-Répcelak field (Pannonian Basin) using stable H, C and O isotope compositions: Implication for mineral storage of carbon-dioxide. *Chem. Geol.* **2021**, *584*, 120536. [[CrossRef](#)]
159. Baker, J.C.; Bai, G.P.; Hamilton, P.J.; Golding, S.D.; Keene, J.B. Continental-scale magmatic carbon-dioxide seepage recorded by Dawsonite in the Bowen-Gunnedah-Sydney Basin System, eastern Australia. *J. Sediment. Res.* **1995**, *65*, 522–530.
160. Moore, J.; Adams, M.; Allis, R.; Lutz, S.; Rauzi, S. Mineralogical and geochemical consequences of the long-term presence of CO₂ in natural reservoirs: An example from the Springerville–St. Johns Field, Arizona, and New Mexico, U.S.A. *Chem. Geol.* **2005**, *217*, 365–385. [[CrossRef](#)]
161. Smith, J.W.; Young, N.B. Dawsonite: Its geochemistry, thermal behavior, and extraction from Green River oil shale. *Colo. Sch. Mines Q. Rep.* **1975**, *70*, 69–93.

Disclaimer/Publisher’s Note: The statements, opinions and data contained in all publications are solely those of the individual author(s) and contributor(s) and not of MDPI and/or the editor(s). MDPI and/or the editor(s) disclaim responsibility for any injury to people or property resulting from any ideas, methods, instructions or products referred to in the content.